



SAPIENZA
UNIVERSITÀ DI ROMA

FACULTY OF MATHEMATICAL, PHYSICAL AND NATURAL SCIENCES
MASTER DEGREE IN PHYSICS
PHYSICS LABORATORY II

Optical read-out characterisation of a Triple-GEM detector

Supervisor

Prof. Gianluca Cavoto

Tutors

Dr. Michela Marafini
Dr. Cecilia Voena

Authors

Lukas Allwicher
Alessandro Bochetti
Mattia Campana
Flavio Di Clemente
Riccardo Mottarelli
Federico Silvetti

Abstract

The aim of this experiment was the characterisation of a Triple-GEM detector, optically read out by a photo-multiplier tube and a multi-pixel photon counter. Different radiation sources have been used to study the produced signals and the timing response of the apparatus. An estimate for the time resolution and the electron drift velocity was extracted from the experimental data. Moreover, a Geant4 simulation for a muon trigger system was carried out and its results compared to the measurements.

academic year 2017-2018

Contents

| | |
|---|-----------|
| Overview | 5 |
| 1 Gas Electron Multiplier and optical reading | 7 |
| 1.1 Gas Electron Multiplier (GEM) | 7 |
| 1.1.1 Operating principle | 7 |
| 1.1.2 Triple-GEM set-up and optical readout | 8 |
| 1.2 MPPC: operating principles | 9 |
| 1.2.1 Introduction | 9 |
| 1.2.2 APD: avalanche multiplication | 9 |
| 2 Experimental set-up | 11 |
| 2.1 Electronic equipment | 12 |
| 2.1.1 High Voltage modules and <i>LabView</i> control software | 12 |
| 2.1.2 NIM modules & co. | 14 |
| 2.1.3 DRS and DAQ software | 15 |
| 2.2 Trigger | 16 |
| 2.2.1 PMT voltage work point set up | 17 |
| 2.2.2 Discriminator thresholds calibration | 17 |
| 2.2.3 Cosmic ray rate assessment | 19 |
| 2.2.4 Random coincidence verification | 20 |
| 2.2.5 Trigger stability | 21 |
| 2.3 Readout apparatuses | 22 |
| 2.3.1 PMT: Cherenkov light | 22 |
| 2.3.2 PMT: single photo-electron charge | 23 |
| 2.3.3 MPPC 13360-6050CS | 24 |
| 2.4 Gas management | 27 |
| 3 Geant4 simulation | 29 |
| 3.1 Simulation of the experiment | 29 |
| 3.2 Analysis and results of the simulation | 30 |
| 3.2.1 Trigger rate in the simulation | 30 |
| 3.2.2 Comparison of energy distributions in simulation and data | 31 |
| 4 Measurements | 33 |
| 4.1 PMT: Review of detected signals | 33 |
| 4.1.1 Signals detected with external trigger | 33 |
| 4.1.2 Signals in auto-trigger mode | 34 |
| 4.2 V_{GEM} scan: readout with PMT | 36 |
| 4.2.1 Photo-electron counts | 36 |
| 4.2.2 Distinction between δ -signals and hotspots | 36 |
| 4.3 E_{drift} scan: readout with PMT | 37 |
| 4.3.1 Signal width and electron drift speed | 37 |
| 4.3.2 Signal timing | 39 |
| 4.3.3 Photo-electron counts | 40 |
| 4.4 MPPC calibration | 41 |
| 4.4.1 Dark noise | 41 |
| 4.4.2 Gain and RC filter | 42 |

| | |
|---|-----------|
| 5 Results | 45 |
| 5.1 Cosmic ray rate | 45 |
| 5.2 Single photo-electron charge | 45 |
| 5.3 Timing of the GEM+PMT apparatus | 45 |
| 5.4 Results in MPPC calibration | 46 |
| Conclusions | 47 |
| A Recovery of a GEM layer | 49 |
| Bibliography | 50 |

Overview

ORANGE (Optical ReAdout Gas Electron multiplier) is a Triple-GEM (Gas Electron Multiplier) detector optically read out and its main goal is the tracking of charged radiation. Thus, the photons coming from the de-excitation processes of the gas molecules inside the detector chamber are revealed, instead of collecting the multiplied electrons. This has several advantages, among which the possibility of decoupling the readout electronics from the detector and the fact that photons aren't affected by the electric fields needed to operate the GEMs.

The read-out apparatuses of the detector were a photo-multiplier tube (PMT) and a multi-pixel photon counter (MPPC). The first was used to study the behaviour of the detector. In particular, the shape of different signals produced by the GEM foils has been analysed, and whether it is possible to distinguish between signals from different sources. The radiation sources used in this search were muons from secondary cosmic rays and electrons from natural radioactivity. Moreover, the timing response of the whole experimental set-up was studied by measuring its time resolution and the average signal duration. This was accomplished using only cosmic muons, which were selected via an external trigger system based on plastic scintillating bars and PMTs. A simulation of this muon trigger system was performed, using the Geant4 toolkit, to obtain a reference for the trigger rate and to check the correct functioning of the apparatus. The MPPC, newly introduced in this year's iteration of the experiment, was calibrated and installed inside the detector housing. However, measurements with this new device, aimed to characterise its interaction with the detector and to compare it to the PMT, couldn't be carried out because of technical problems encountered before the actual data taking. Nevertheless, some considerations could be made on its use in an optically read out GEM system.

Chapter 1

Gas Electron Multiplier and optical reading

In this chapter we will briefly introduce the main components of the experimental apparatus and their operating principles.

1.1 Gas Electron Multiplier (GEM)

A Gas Electron Multiplier is a type of Micro pattern gas detector introduced in the late Nineties as a new tool able to ensure high gain and fast detection, along with the ability of tracking multiple particles [1].

1.1.1 Operating principle

The fundamental component of the device is a thin foil of insulating material, usually Kapton[®], sandwiched between two coatings of conducting copper. Microscopic holes (around $70\text{ }\mu\text{m}$ in diameter) are then drilled into the foil by means of chemical etching, covering up to 30% of the total surface. The manufacturing process is tailored to produce holes in a typical double-conical shape.

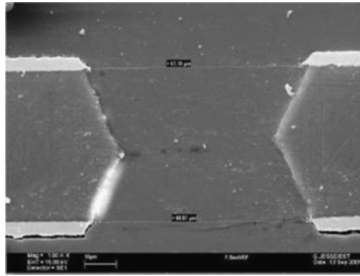
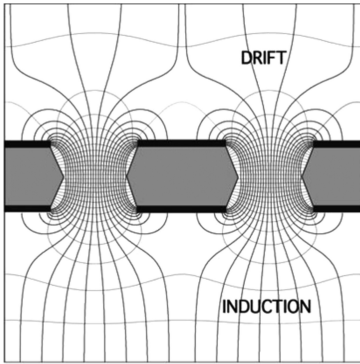


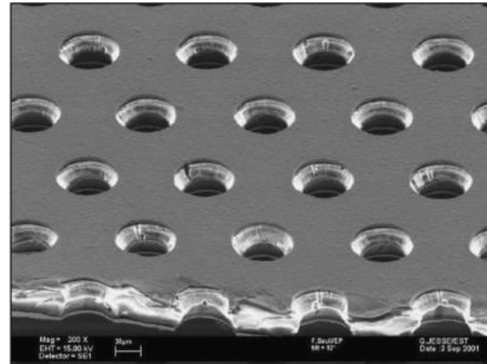
Figure 1.1: Example of the double-conical shape of a single GEM hole.

Lastly, the foil is mounted between two electrodes and the entire device is put under a controlled atmosphere with a scintillating gas and a quencher (in our case Helium and Carbon tetrafluoride). When a voltage is applied to the faces of the foil and to the external electrodes three different electrical fields are formed, as shown in figure (1.2a).

- 1 A *drift field* (about 1 kV/cm), from the cathode to the closest face of the GEM foil, used to drive the electrons emerging from ionisation processes due to radioactivity toward the holes in the GEM.
- 2 A *GEM field* (about 100 kV/cm), inside the holes of the foil. The geometrical configuration of the holes allows to generate an intense field capable of multiplying the electrons in an avalanche mechanism.
- 3 An *induction field* (about 1 kV/cm), used to guide the emerging electrons toward the anode for signal pick-up and readout.



(a) Schematic drawing of the fields around a single layer GEM.



(b) Image of the microscopic structure of a GEM foil.

Figure 1.2: Images from [1]

1.1.2 Triple-GEM set-up and optical readout

In order to achieve greater gain, the base structure elucidated in §1.1.1 can be replicated using multiple foils in sequence. Indeed, our apparatus was made up of three square GEM layers, each $10 \times 10 \text{ cm}^2$ in size. Each layer is separated from the next by a transfer gap of 2 mm. In these regions, the difference in voltage between the foils establishes a *transfer field* of around 1 kV/cm that carries the electrons from one layer to the next. The drift gap between the cathode and the first GEM layer is 3 mm high.

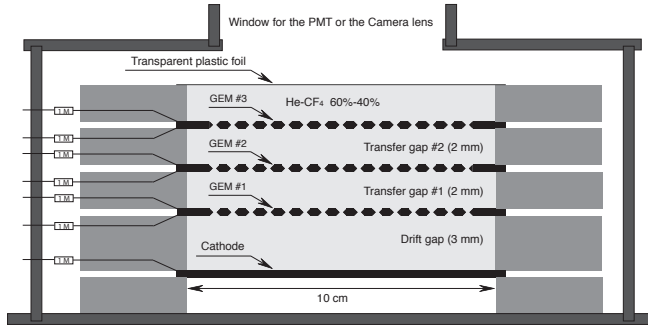


Figure 1.3: Schematic view of the Triple-GEM set-up. Taken from [2], in which the same detector was operated with the 60:40 He:CF4 mixture.

The ionisation processes taking place in the last GEM stage and in the induction gap above it also produce photons thanks to the excitation and de-excitation of the gas molecules. Depending on the mixture used in the GEM atmosphere, this light emission is located in the optical and near-optical spectra. These photons can be seen using a suitable light detector, such as a PMT, a MPPC or a CMOS unit. The first two options enable an energy release measurement independent from the electron collection, while the last one provides a way to track ionising particles inside the GEM (see [2, 3, 4, 5]). The main advantages of this approach are the decoupling between electronics and detection media, intrinsic multiple hit capability in tracking applications and high light yield thanks to the GEM large gain and optical transparency [6].

The aim of our experiment was to examine the de-excitation light from the gas mixture of He:CF4 in 40:60 proportion inside the GEM chamber. The radiation sources used to study the detector were secondary cosmic radiation (i.e. muons, for their close to minimum energy release by ionisation inside matter [7]) and other background phenomena (i.e. δ rays from natural radioactivity). In order to do so, the apparatus had to be modified to allow the read-out of photons from the last amplification stage. This was implemented by removing the anode from the stack and replacing it with a transparent window. Thus, in our set-up, no induction field was present and the topmost copper layer was grounded in order to carry away the ionisation electrons. The He:CF4 mixture was chosen for its high gain capabilities in high voltage applications (see Figure (1.4a)). Moreover carbon tetra-fluoride is known to be a fast

scintillator and to generate low electron diffusion [8]. We were forced to use a 40:60 mixture, which has a lower light yield than the 60:40 (Figure (1.4b)), because of technical problems in the gas circulation system of the laboratory. We expect this mixture to have two emission bands between $200 \sim 350$ nm and $500 \sim 800$ nm [8], which can be used for optical reading, depending on the spectral response of the readout device.

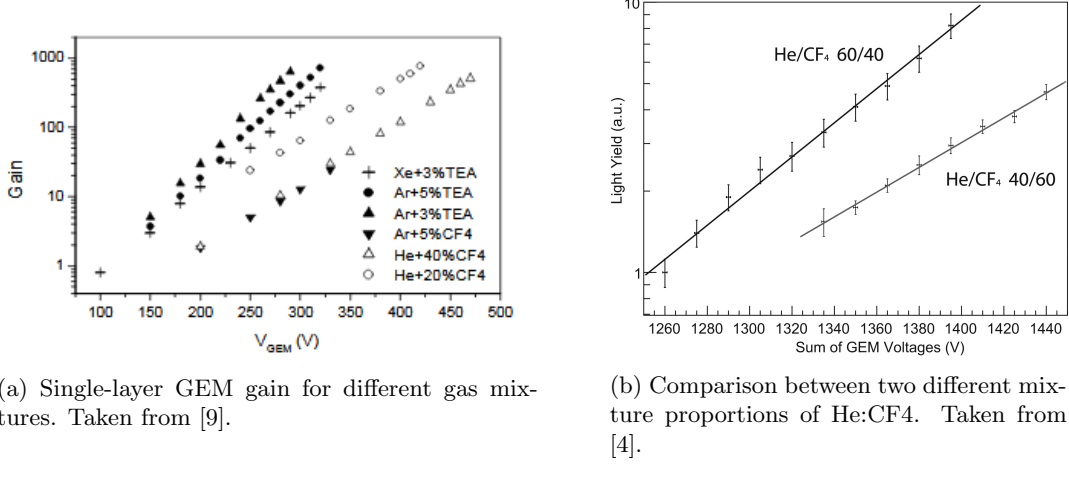


Figure 1.4

1.2 MPPC: operating principles

1.2.1 Introduction

The MPPC (Multi-Pixel Photon Counter) is a device from the SiPM (Silicon Photo-Multiplier) family. It uses multiple APDs (Avalanche Photo-Diodes) operating in Geiger mode, each combined to a quenching resistor. The MPPC is very useful for the detection of extremely weak light at the photon counting level. It operates on a low voltage and features high gain, high efficiency, fast response and wide spectral response range. It is also immune to magnetic fields, highly resistant to mechanical shocks, and does not suffer from “burn-in” by incident light saturation.

1.2.2 APD: avalanche multiplication

The photo-current generation mechanism of the APD is the same as that of a normal photo-diode. When light enters the APD, electron-hole pairs are generated if the light energy is higher than the band gap energy. When the electron-hole pair is generated inside the depletion layer of an APD with a reverse voltage applied to the P-N junction, the electric field created across the junction causes the electrons to drift toward the N side and the holes to drift toward the P side. The higher the electric field strength, the higher the drift speed of these carriers. When the electric field reaches a certain level, the carriers are more likely to collide with the crystal lattice, ionising the atom of the lattice and then generating a new electron-hole pair. This chain reaction of ionisations is known as avalanche multiplication (Geiger mode). The characteristic curve for an APD is shown in Figure (1.5).

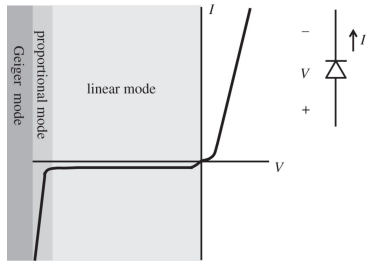


Figure 1.5: APD characteristic curve.

Chapter 2

Experimental set-up

The experimental apparatus was composed by several parts:

- Two scintillating bars, each equipped with a photomultiplier tube, which were used to build a trigger system for muons from secondary cosmic rays.
- A GEM with three layers, adapted for optical reading as described in the previous chapter.
- A photomultiplier tube, mounted on top of the GEM in order to receive the de-excitation light from the gas mixture.
- A MPPC, also used for optical reading.
- A NIM crate containing the necessary modules for signal management and for supplying power to the PMTs and the GEM.
- Two DRS evaluation boards, used for data acquisition.
- A gas circulation system composed of a tank of He:CF4 mixture in 40:60 proportion with a remote controlled valve and suitable tubing.

Moreover, we used a Tektronix TDS 360 digital oscilloscope and a Fluke 8050A digital multimeter for signal monitoring and all measurements relative to the experiment set-up.



Figure 2.1: Experimental set-up. The GEM and its read-out PMT are placed between the two scintillators of the trigger system. The MPPC is mounted directly inside the GEM box.

2.1 Electronic equipment

2.1.1 High Voltage modules and *LabView* control software

For the experiment we had two *CAEN N1470* HV supply modules and one *CAEN N472*; the major difference between the two is the possibility to control the voltages of the first one with the computer via a USB port. The *N472* module has 4 channels and each one can be set to a different voltage, adjustable with a manual screw. The *N1470* also has 4 channels, but each one can be set to remote or local control. In remote mode the module is interfaced with a computer via USB port and receives its instructions from an appropriate *LabView* environment. Custom *LabView* functions, called *SubVIs*, provided by the HV modules' manufacturer, are used to manage the channel. In local control, instead, the voltage has to be set up manually.

Moreover, the *N1470* module has the *ramp up*, *ramp down* and *kill* modes, so that it is possible to bring the voltage up and down gradually with the first two, and, if necessary, to bring it down rapidly in a controlled way with the last one.

In order to make the detector work in optimal conditions, it is necessary to apply precise voltages among the GEM foils and between two sides of a single foil. The first ones are needed to establish a *drift field* (E_{drift}) between the cathode and the first GEM foil, and two *transfer fields* (E_{T1} , E_{T2}) between the other GEM foils. To accomplish this, it has been necessary to take advantage of the software developed for the same purpose in the previous iteration of the experiment, which is described in detail in [10]. This software is capable of supplying voltage to the seven HV channels connected to the detector and it ensures that each one meets the correct values for maintaining the desired electric fields in the detector. Given the importance of these voltage values, they are reported here briefly:

- $V_{G3D} = 0 \text{ V}$
- $V_{G3U} = V_{G3D} + \Delta V_3$
- $V_{G2D} = V_{G3U} + E_{T1} \cdot 0.2\text{cm}$
- $V_{G2U} = V_{G2D} + \Delta V_2$
- $V_{G1D} = V_{G2U} + E_{T2} \cdot 0.2\text{cm}$
- $V_{G1U} = V_{G1D} + \Delta V_1$
- $V_{drift} = V_{G1U} + E_D \cdot 0.3\text{cm}$

where with ΔV_X , V_{GXD} and V_{GXU} we indicated respectively the voltage between the surfaces, the down surface and the high surface of the *GEM_X* (going from bottom to top $X = 1, 2, 3$). The multiplicative factors, 0.2 cm and 0.3 cm, are, respectively, the distance between the GEM foils and the distance between the first foil and the cathode (see Figure (1.3)). All electric fields are expressed in V/cm.

Since one of the four channels of the *CAEN N472* module was broken and the other three were needed to power the PMTs of the muon trigger system (see §2.2), it was necessary to use the remaining channel of the two *N1470* modules to supply the read-out PMT. So, a software has been implemented to monitor the voltage and current supplied to the PMT, which is described in the section below.

LabView software description

First, it was necessary to ensure that the program initialised the module's address properly. This was done using a initialisation function, which established the communication with the module specified in the *VISA Resource Name*, and another one which allowed us to access the module's settings, accepting as argument the module's local bus address (manually set from the module on board control panel). Both these *SubVIs* were provided by *CAEN*.

The next step was to set up operations in order to monitor the general behaviour of the module, like the *ramp up*, the *ramp down* and the *trip* modes. The trip, in particular, is the state in which the monitored current is higher than the maximum allowed value for a certain amount of time, for some HV channel. Both the current limit and the time interval are established *a priori*. The *ramp up* and *ramp down* velocities were set at 20 V/s and 100 V/s, exactly the same as those used to raise and lower the GEM foils.

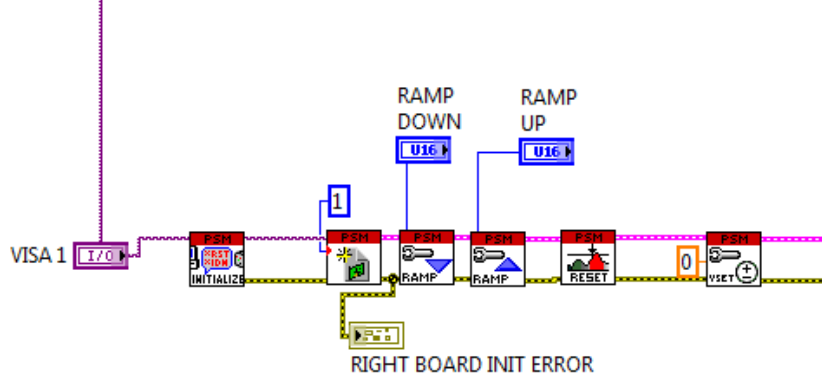


Figure 2.2: The initialisation sequence.

At the end of the initialisation two *SubVIs* were placed, one to clear all the error messages, so that it was possible to turn on all the channels, the other to reset the value of all channels to 0 V. Figure (2.2) shows the *SubVI* sequence that executes the module's initialisation.

Once the module initialisation was completed, the program entered the main work cycle, that contained all the *SubVIs* handling the PMT channel. Upon changing the “ON/OFF” button’s status, the program executed the following instruction sequence to all channels:

- 1 The channel is turned on and begins the work cycle.
- 2 In the first iteration of the work cycle, the maximum voltage and the maximum current (V_{max} and I_{max}) are set to the default values. In the following iterations the program does not execute this operation unless the user wants it to be executed, and in this case he has to set up the V_{max} and I_{max} by pressing the button “MAX V/I”.
- 3 The status of the channel is monitored.
- 4 The value of the voltage given by the instrument is read. If it is compatible in a 20 V range with the one set by the user “VNOM”, the program reports the correct running of the channel by turning the “V OK!” indicator on. If the tension is higher, the anomaly is instead notified by turning on the “OVV” indicator.
- 5 The program reads the value of the current that circulates effectively in the channel and, if it is higher than 20% of I_{max} , it reports the anomaly. If it exceeds the value of I_{max} the program gives an “OVC” alarm for 5 seconds and then executes the trip mode for the channel.
- 6 The program restarts from point (2).

The front panel (Figure (2.3)) showed the voltage and current measurements retrieved from the HV module. A LED indicator (“V OK!”) was added to point out that the applied voltage is within the suitable range. If instead the value did not fit in the decided range, the “OVV” LED switched on, reporting the anomaly to the user.

The work cycle could be interrupted by pressing either the “ON/OFF” or the “FERMA TUTTO” button. If the value of “ON/OFF” was changed, the program exited the work cycle, the channel was disabled, the voltage brought to zero at *ramp down* velocity and possible error messages registered by the modules were reported; then the user could close the program or restart the work cycle. If the channel reported a current higher than the maximum value (I_{max}) for more than 5s, the channel entered the *trip* mode, turning off the channel and stopping the work cycle. The module would then stay in the alarm status until the button “CLEAR ALARM” were pressed. During this time, it would be impossible to rehabilitate the channel and restart the work cycle.

It is possible to insert some instructions in the *while* cycle and some *if-else* conditions in the LabView environment. Some *SubVIs* in the work cycle were executed only if some conditions were verified, in order to maximise the efficiency of the program in terms of execution speed. The work cycle (Figure (2.4)) consisted of 3 main *if-else* blocks. The first one contained all the necessary instructions to set up

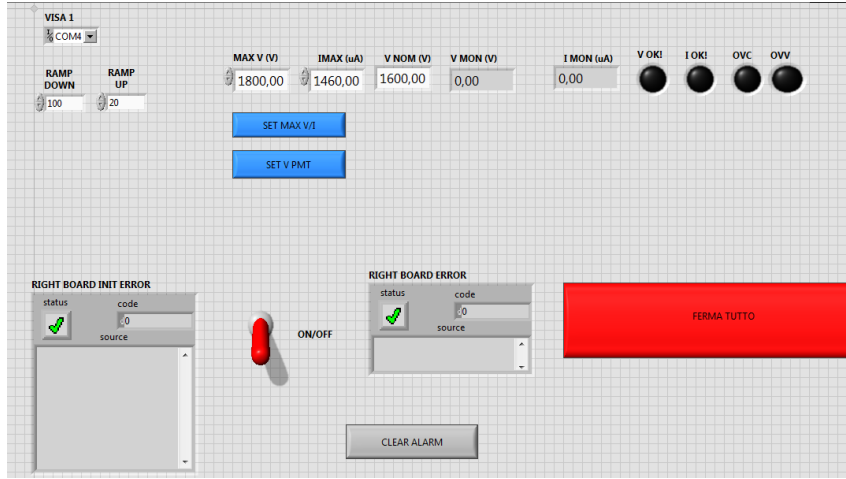


Figure 2.3: The front panel.

the maximum voltage and the maximum current in the channel, and it was executed only after the user pressed the “*SET MAX V/I*” button. The second one allowed to change the voltage applied to the PMT and corresponded to the button “*SET V PMT*”. The third one contained all the *SubVIs* that read the state of the channel and the corresponding voltage, reporting possible anomalous values (*OVV*, *OVC* and *TRIP*) and the linked error status. The last one was executed until the work cycle was running.

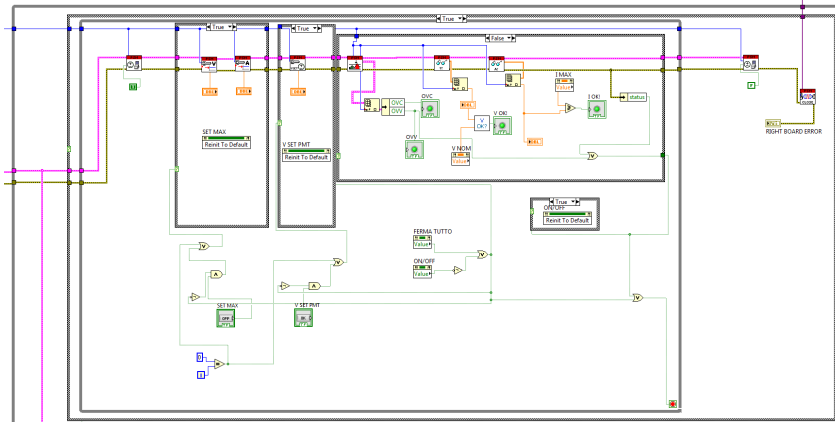


Figure 2.4: Work cycle.

As we can see in Figure (2.4), the work cycle was a *do-while* cycle, terminated by a *stop if true* condition, to which the “*ON/OFF*” (taking the NOT because it works in reverse logic respect of the arrest button) and “*FERMA TUTTO*” commands were linked. When one of the two buttons was pressed the cycle did not end immediately, but it executed one more iteration, since the indicators were not updated instantaneously. In order to minimise the turn off time, a series of logic operators prevented the access to the *if-else* block, as it is possible to see again in Figure (2.5). In the eventuality that one of the channels presented an error, the program was stopped by an instruction that switched the “*ON/OFF*” value to OFF.

2.1.2 NIM modules & co.

All the electronic modules at our disposal were mounted on a NIM crate, as shown in Figure (2.6). These were used both for the trigger system and for general signal routing and attenuation. We will now make a short review of the modules and their purpose in the experiment.

- *CAEN mod.96 8 CHS Discriminator*, used to convert the signals coming from the scintillator PMTs into digital signals that could be evaluated by the coincidence unit. The threshold voltage could be varied between 20 mV and 380 mV, and the pulse lenght in the range [7, 300] ns.

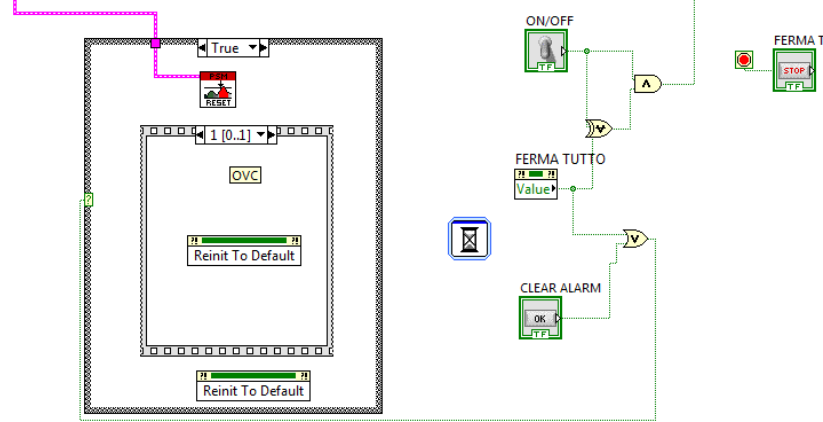


Figure 2.5: Logic operators.

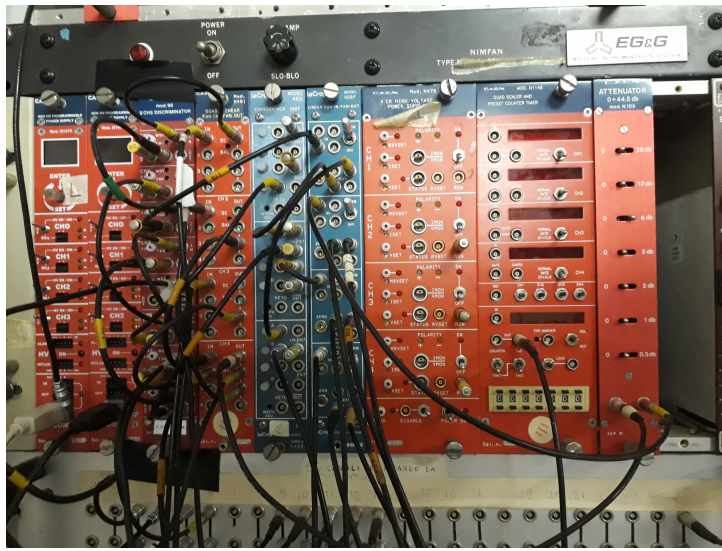


Figure 2.6: NIM crate with mounted modules.

- *LeCroy MODEL 465 COINCIDENCE UNIT*. This was our logical unit for coincidence evaluation in the trigger system. It had three channels with 4 inputs each
- *CAEN mod.N401 QUAD LINEAR FAN IN-FAN OUT* and *LeCroy MODEL 428F LINEAR FAN IN-FAN OUT*, to duplicate or sum signals.
- *CAEN mod.N1145 QUAD SCALER AND PRESET COUNTER TIMER*. This module was used as a counter in the calibration of the trigger system components.
- Two *CAEN mod.N109 ATTENUATORS* were used to attenuate the signals coming from the read-out PMT and the MPPC, in order to adjust them to the input range of the DRS evaluation boards. The attenuation could be set between 0 dB and -44.5 dB.
- *70 ns delay channels*. This rack-mounted module, visible in the lower side of Figure (2.6), was used to delay the trigger signal from the coincidence unit, in order to circumvent the “software” delay of the data acquisition program, which had some flaws affecting the signal baseline stability.

2.1.3 DRS and DAQ software

The *DRS4 evaluation board* is a 4-channel data acquisition board based on the DRS4 chip, designed at Paul Scherrer Institut in Switzerland, capable of digitising at up to 5 GS/s with 1024 sampling points and a 14-bit ADC [11]. The four AC-coupled analog input channels have an input range of 1 V, from -500 mV to 500 mV. Since all relevant signals in the experiment were negative and in some case exceeded

-500 mV, it was necessary to introduce an attenuator into the signal flow to acquire them. The board is powered via USB, through which also the data transfer takes place at more than 20 MB/s. Moreover, there is an on-board trigger logic, used to start the acquisition at the right time.

The board was installed on a Linux machine, where the DAQ program, written in C++, controlled all the possible launch options of the DRS. For example, the trigger threshold or the delay of the acquisition with respect to the trigger time are two of these options. It could also be set whether the acquisition should run for a given time or for a given number of events. Every event was a $\sim 1\ \mu\text{s}$ long time window, in which 1024 points for each acquired channel were stored in a bi-dimensional array. All the data were then saved in a ROOT tree for further off-line analysis.

2.2 Trigger

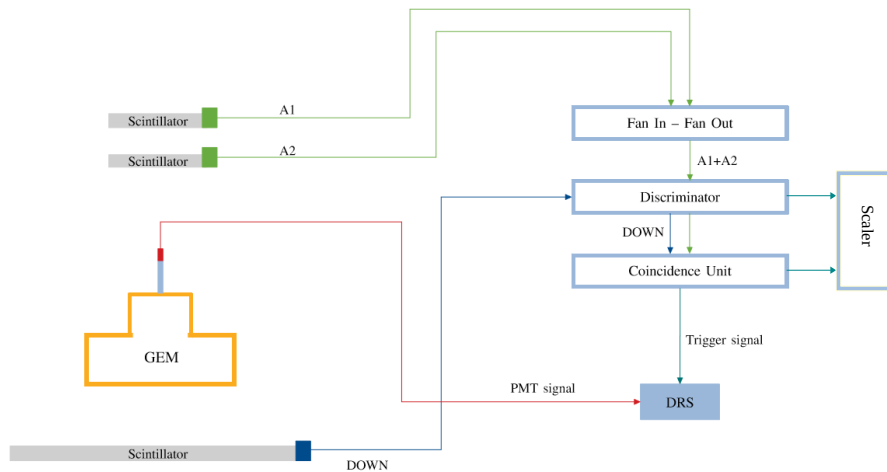


Figure 2.7: Schematic view of the muon trigger system.

The topic of this section is the set-up of a muon trigger system, used to recognise the arrival of a secondary cosmic ray in the detector. To achieve this, we used three plastic scintillators, each coupled to its own photomultiplier tube.

Two of these ($A1, A2$) were already packaged together as a single unit, which was placed on top of the GEM. The third one (*down*) was instead placed below, as shown in Figures (2.1) and (2.7). The sizes of these objects were measured and are reported in Table (2.1).

| | length [cm] | width [cm] | height [cm] |
|---------------|-------------|------------|-------------|
| Down | 70.0 | 13.0 | 3.0 |
| A1, A2 | 10.0 | 13.0 | 1.0 |

Table 2.1: Sizes of the scintillators used in the trigger system. All measurements are accurate up to an error of ± 0.5 cm. Note that the *down* scintillator is about seven times larger than the other two.

Due to geometrical constraints in the support structures for the apparatus, the upper scintillators had to be rotated of 45° in order to be stable. The signals from the two upper scintillators were sent to a *fan in-fan out* unit to be summed, then both outputs from *down* and $A1+A2$ were converted into

NIM logic signals by using a chain of two discriminator units ¹. After this step, the discriminated signals were processed in a coincidence unit to obtain the sought trigger signal.

In order to optimise the performance of the system, the operational voltages for each PMT and the discriminator thresholds had to be searched. Therefore, the scintillators were placed directly on top of each other, so that the coincidence rate was maximised, and the counting rate was sampled in various configurations.

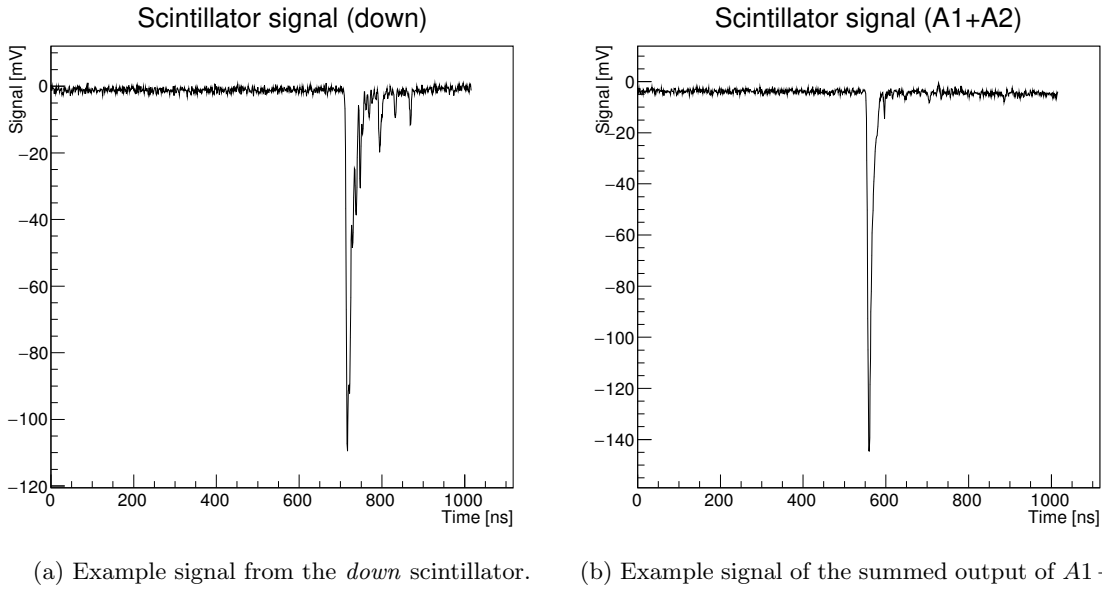


Figure 2.8

2.2.1 PMT voltage work point set up

The optimal voltages necessary to operate the trigger PMTs were studied by measuring the coincidence counting of two units, keeping the power supply of one fixed while varying the other. The aim of this process was to identify which voltage guaranteed the most stable PMT response. This helps in separating the signals generated by the scintillation from the muons from spurious noise signals.

For the *down* scintillator, this search was initially carried out in coincidence with an extra scintillator+PMT unit left from the previous year, which was later discarded from the experiment when *A1* and *A2* became available.

The voltage applied to the *down* photo-tube swept a range between $[-2500, -1600]$ V. Eventually, the choice for the optimal voltage, V_{down} , was made by selecting the point where the number of counts stopped increasing, as can be seen in Figure (2.9). Thus, the working point was fixed at

$$V_{\text{down}} = -1975 \text{ V}. \quad (2.1)$$

The same procedure was repeated for both *A1* and *A2* scintillators in the range $[-1600, -1000]$ V. Each one was set up in coincidence with the *down* scintillator, which was already operated at the work point found previously. The corresponding plots are omitted since the pattern is similar to the one of Figure (2.9). As a result, both were set at $V_A = -1450$ V for the remainder of the work.

2.2.2 Discriminator thresholds calibration

In order to set the optimal threshold for each discriminator unit the coincidence counts were examined.

The effect of a stricter threshold is to reduce the overall counting rate from the coincidence unit, as both noise and real signal are rejected. Similarly, if the discriminator threshold is too low, the contribution to the trigger rate from noise is expected to increase. The optimal value should guarantee a compromise between these extreme situations.

¹The daisy chaining of multiple discriminators was necessary due to the age and signal instability of the equipment.

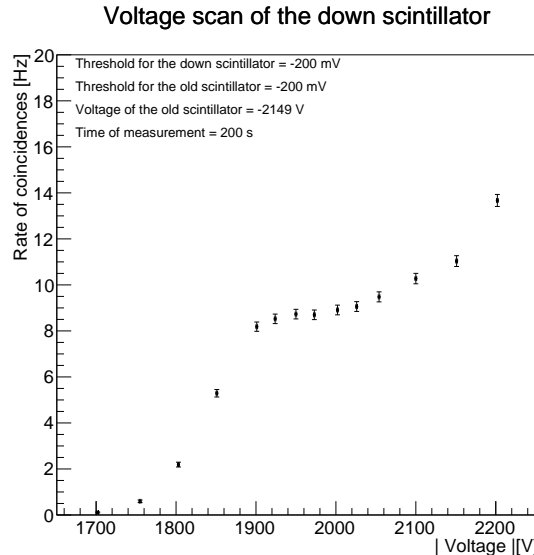


Figure 2.9: Voltage scan for V_{down} . The counting rate becomes stable at the *plateau* around 1900 V.

As for the PMT voltage scan, the *down* scintillator was set in coincidence with the left-over scintillator+PMT unit, which was kept at fixed voltage and discriminator threshold. Then the coincidence counts sampled at various threshold values for intervals of 200 s.

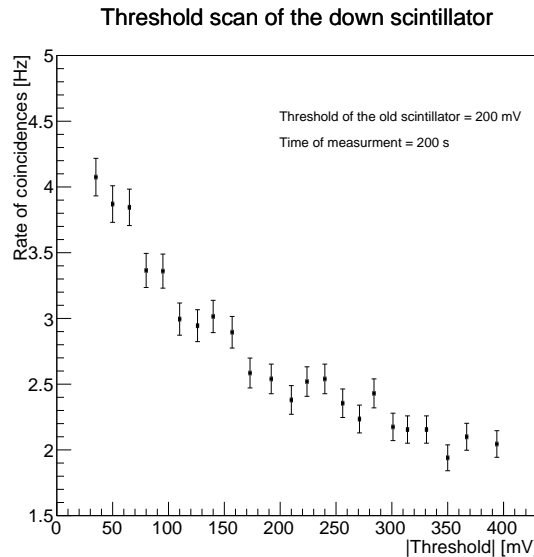


Figure 2.10: Threshold scan for the *down* scintillator.

By looking at Figure (2.10), it was chosen to set the threshold at -180 mV. For the upper part of the trigger system, the same procedure was repeated individually for $A1$ and $A2$, by counting the coincidences with *down*. This way, two temporary values $V_{t,A1} = -150$ mV and $V_{t,A2} = -115$ mV were fixed. Then, the same search was repeated one last time for the coincidences of the summed signal $A1 + A2$ with *down*, which was our actual trigger configuration. The threshold for this signal was chosen at $V_{t,sum} = -225$ mV. At this point, the sum counted roughly as many coincidences as the single $A1$ and $A2$ scintillators. Again, the plots are **not shown for the sake of brevity**.

Finally, the work point for the entire trigger system was fixed at

| | $\mathbf{V}_{\text{supply}} [\text{V}]$ | $\mathbf{V}_{\text{threshold}} [\text{mV}]$ |
|--------------|---|---|
| Down | -1950 | -180 |
| A1+A2 | -1450 | -225 |

2.2.3 Cosmic ray rate assessment

An estimation of the trigger rate was developed by considering the integral

$$R = \int_D F(\theta) dx dy d\cos(\theta) d\phi. \quad (2.2)$$

The dominion of integration D spans the entire surface of the lower scintillator in the variable x, y and all the rays that cross the surface of the upper scintillor in the spherical coordinates $\cos(\theta), \phi$. The muon flux density on a horizontal surface has been parametrised as

$$F(\theta) = F_0 \cos^3(\theta), \quad \text{with} \quad F_0 = 70 \frac{\text{ev}}{m^2 s \text{ st}}, \quad (2.3)$$

as reported by [7].

Initially, the rate for the test configuration with the scintillators positioned on top of each other was computed directly.

$$R_{\text{close, teo}} = \int_0^a \int_0^b \int_0^{\pi/2} \int_{-\pi}^{\pi} 4F(\theta) \sin(\theta) d\phi d\theta dy dx \rightarrow \frac{8}{3}\pi ab F_0 = (1.91 \pm 0.04) \text{ Hz}. \quad (2.4)$$

Where $a = (6.5 \pm 0.25)$ cm and $b = (5 \pm 0.25)$ cm are half the lengths of the sides of the scintillators A1 and A2. Moreover, the heights of all scintillators were neglected. An experimental measure of the trigger rate in these conditions was

$$R_{\text{close, exp}} = (1.51 \pm 0.12) \text{ Hz}. \quad (2.5)$$

So, in this configuration, the measure is compatible with the theoretical prediction.

The next step was to evaluate the trigger rate in the geometric configuration for the actual experiment. Thus, the centres of the scintillators *down* and *A11+A2* were aligned and separated of a vertical distance $h = (46.5 \pm 0.5)$ cm, as shown in Figure (2.1).

For this geometry the integration of (2.2) would have been quite cumbersome, so a few simplification were introduced. First, the upper scintillator shape was approximated with a circle of radius $\rho = \sqrt{\frac{4ab}{\pi}} = (6.4 \pm 0.2)$ cm. Second, it has also been assumed that, since the geometrical centres of both surfaces were aligned vertically, the computation was symmetric in the x, y variables. Lastly, the thickness of both objects has been neglected. These manipulations allow to divide the integral into four contributions

$$\begin{aligned} R = & 4 \left[\int_0^\rho \int_0^{\sqrt{\rho^2 - x^2}} \int_0^{\Theta_1(x,y)} 2\pi F(\theta) \sin(\theta) d\theta dy dx + \right. \\ & + \int_0^\rho \int_0^{\sqrt{\rho^2 - x^2}} \int_{\Theta_1(x,y)}^{\Theta_2(x,y)} \int_{-\Phi(x,y,\theta)}^{\Phi(x,y,\theta)} F(\theta) \sin(\theta) d\phi d\theta dy dx + \\ & + \int_0^\rho \int_{\sqrt{\rho^2 - x^2}}^B \int_{\Theta_1(x,y)}^{\Theta_2(x,y)} \int_{-\Phi(x,y,\theta)}^{\Phi(x,y,\theta)} F(\theta) \sin(\theta) d\phi d\theta dy dx + \\ & \left. + \int_\rho^A \int_0^B \int_{\Theta_1(x,y)}^{\Theta_2(x,y)} \int_{-\Phi(x,y,\theta)}^{\Phi(x,y,\theta)} F(\theta) \sin(\theta) d\phi d\theta dy dx \right]. \end{aligned}$$

Where $A = (5 \pm 0.25)$ cm and $B = (34.5 \pm 0.25)$ cm are half the length of the lower scintillator sides and the boundaries for the integrals are defined by

$$\begin{aligned}
r &= \sqrt{x^2 + y^2}, \\
\Theta_1(x, y) &= \arccos \left(\frac{h}{\sqrt{h^2 + (\rho - r)^2}} \right), \\
\Theta_2(x, y) &= \arccos \left(\frac{h}{\sqrt{h^2 + (\rho + r)^2}} \right), \\
\Phi(x, y, \theta) &= \arccos \left[\frac{(h \tan(\theta))^2 + r^2 - \rho^2}{2hr \tan(\theta)} \right].
\end{aligned}$$

A graphical representation of the same boundaries is shown in Figure (2.11).

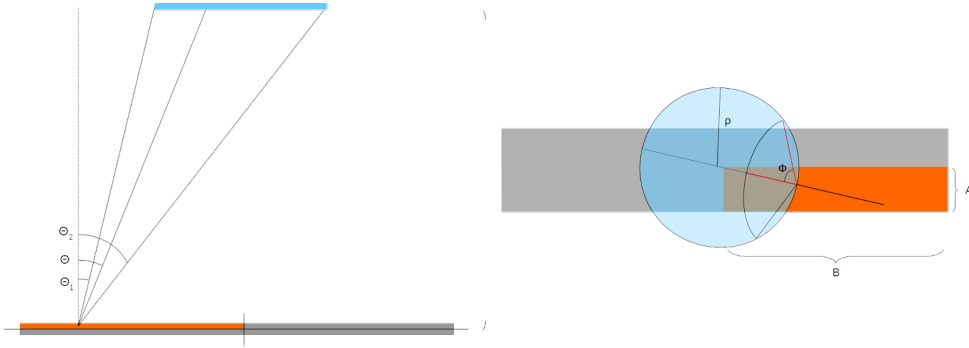


Figure 2.11: Scheme of the integration boundaries for a generic point (x, y) in the orange region. The remaining grey part is symmetric to the former one. Figures are not in scale.

The integrals in previous formula were evaluated numerically, and an error was assigned by repeating the computation several times, each varying a parameter, $p \in \{\rho, A, B, h\}$ between $p \pm \sigma_p$ and modifying the integration boundaries accordingly. The error contributions were then summed finding the estimate

$$R_{\text{teo}} = R \pm \sum_p \frac{R_{p+\sigma_p} - R_{p-\sigma_p}}{2} = (0.24 \pm 0.03) \text{ Hz}. \quad (2.6)$$

The experimental trigger rate in this configuration was measured to be

$$R_{\text{exp}} = (0.363 \pm 0.002) \text{ Hz}. \quad (2.7)$$

So one can conclude that the prediction and the measure are reasonably close even if not within error.

2.2.4 Random coincidence verification

A first verification on the correct functioning of the trigger system was carried out by measuring the rate of random coincidences. In order to do so, the upper scintillators were intentionally displaced and then the count rate of $A1+A2$, *down* and their coincidence were recorded for an interval of 1500 s. Since both NIM signals from the discriminators had a length of $\tau = (125 \pm 1)$ ns, the theoretical rate of random coincidences is expected to be

$$R_{\text{ran, teo}} = 2\tau R_{A1+A2} R_{\text{down}} \rightarrow (3.9 \pm 0.1) \cdot 10^{-5} \text{ Hz}. \quad (2.8)$$

On the other hand, the experimental rate measured for the same data resulted

$$R_{\text{ran, exp}} = (3.6 \pm 0.7) \cdot 10^{-2} \text{ Hz}. \quad (2.9)$$

The large discrepancy between the measured and expected rate of random coincidences suggests the existence of some form of correlated noise between the PMTs used in the trigger system. Given the large value of (2.9), we have subtracted it from the measured trigger rate, obtaining

$$\tilde{R}_{exp} = R_{exp} - R_{ran,exp} = (0.327 \pm 0.007) \text{Hz}.$$

In fact, this number is compatible with the theoretical prediction (2.6) within 3σ .

2.2.5 Trigger stability

In order to ensure the trigger stability, the counting rate of all the scintillators has been measured over time, starting from the moment the HV was turned on. It was found that, while the counting rate for the *A1* and *A2* scintillators was reliable and time-independent, the *down* scintillator was affected by a strong instability. Figure (2.12) shows the progressive stabilisation of the counting rate for this scintillator as a function of time .

An exponential fit has been computed over the plot via the function

$$f(x) = R + B e^{-\frac{x}{T}}$$

obtaining, with a $\frac{\chi^2}{\text{DOF}} = 1,23$

$$\begin{aligned} R &= (81.77 \pm 0.63) \text{ Hz} \\ B &= (69.85 \pm 4.66) \text{ Hz} \\ T &= (264.8 \pm 22.5) \text{ s} \end{aligned}$$

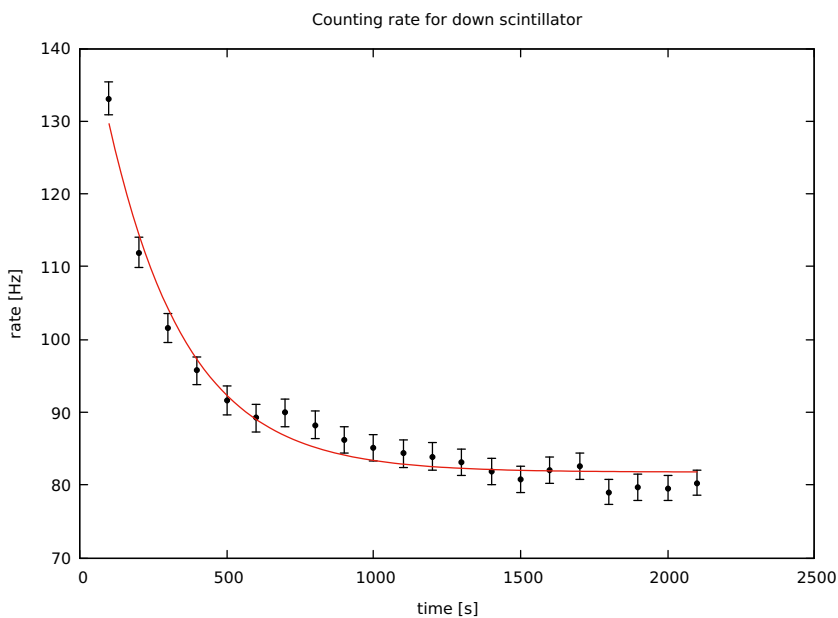


Figure 2.12: Counting rate of the *down* scintillator as a function of time.

Given the fit results, the time constant can be used to compute how much time is needed before the scintillator reaches its stability region. At least $3T$ of time should pass before the use, corresponding approximately to 700 seconds. Thus, we choosed to wait approximately 1200 seconds (20 minutes) seconds after every power on. The stable rate resulting from the fit is $R = (81.77 \pm 0.63) \text{Hz}$. Further measurements, which are not shown for the sake of brevity, have been collected over time and they confirmed the stability of this rate.

2.3 Readout apparatuses

2.3.1 PMT: Cherenkov light

As already shown in Figure (1.3), the readout PMT was mounted on top of the Triple-GEM detector, with its photo-cathode window parallel to the GEM foils, and thus almost orthogonal to the trajectory of the muons crossing both the detector and the trigger system. Whenever the muons also crossed the photo-cathode surface (which is approximately $\frac{1}{5}$ of the detector's surface), another peak originated in the signal due to the Cherenkov light emission in the window. Indeed, this is possible since, assuming the average energy of a cosmic muon to be around 3 GeV (as $\beta \simeq 1$) [7], the Cherenkov emission angle is

$$\theta_C = \arccos\left(\frac{1}{\beta n_w}\right) \simeq \arccos\left(\frac{1}{n_w}\right),$$

where n_w is the refraction index of the photo-cathode window. For the critical angle (θ_0) of the glass-air interface we can write

$$\begin{aligned} \sin(\theta_0) &= \frac{n_{air}}{n_w} = \frac{1}{n_w} \simeq \cos(\theta_C) \\ \Rightarrow \theta_0 &= 90^\circ - \theta_C \leq \theta_C \quad \text{if } n_w \geq \sqrt{2} \simeq 1.41. \end{aligned}$$

Since $\theta_C = \theta_i$, where θ_i is the incident angle of the Cherenkov light on the interface (see Figure (2.13)), the produced light is completely reflected inside the photo-cathode ² and revealed by the PMT. This signal is very narrow (see Figure (2.14) for an example signal without GEM) and, as will be further discussed below, precedes every other signal from the GEM.

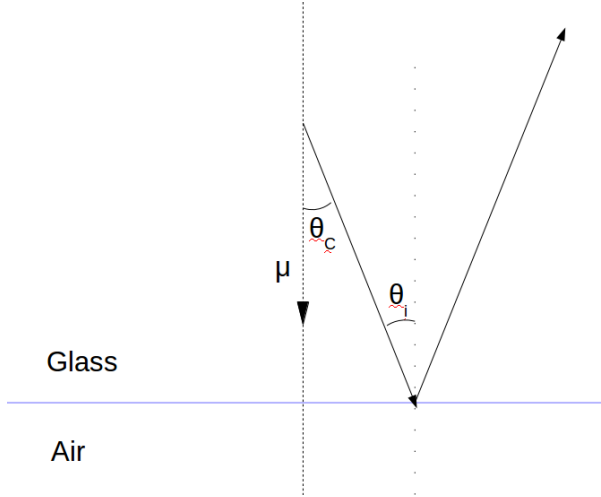


Figure 2.13: Scheme of a vertical muon crossing the photo-cathode window and emitting Cherenkov light.

The discussion above is strictly valid only for completely vertical muons. However, if the trajectory isn't completely normal to the photo-cathode's surface, the effect is that only a part of the produced light can be reflected, since there will be a region in which the incident angle is higher than θ_0 , and this light will be completely reflected. Elsewhere, instead, depending on the inclination of the incoming muon, some of the photons may escape into the detector's encasing. The overall effect will therefore be a smaller, but still detectable, Cherenkov peak, since the trigger configuration doesn't allow for muons at high angle to cross the PMT. To avoid this peak a solution could be to tilt the whole detector slightly, in order to increase the angle of the cosmic rays in the photo-cathode, and moreover reduce the surface exposed to the muon flux, while the effect on the drift volume in the detector would be negligible. However, we have chosen not to do so, as the Cherenkov peaks have a very precise timing, and, as already mentioned, precede the "real" signal we were interested in. Thus, they could be easily filtered out when analysing the data (see §4.3).

²We don't know the exact material of which the photo-cathode window is made, but we can safely assume that, since it's made of some type of glass, the condition $n_w \geq \sqrt{2}$ is verified.

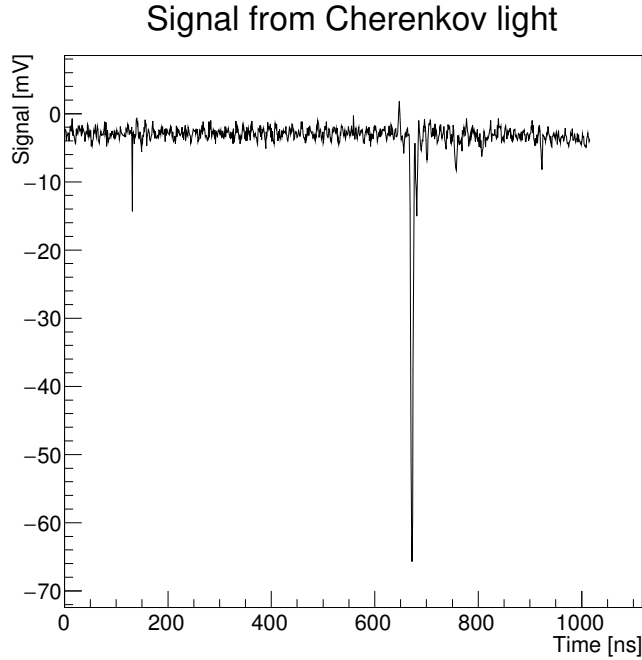


Figure 2.14: Typical signal from cosmic muons crossing the readout PMT’s photo-cathode window (peak at ~ 700 ns).

2.3.2 PMT: single photo-electron charge

The operating voltage for the readout PMT could not be set in the same fashion as those used for the trigger, due to the lack of a suitable scintillating material to use as a source of photons. Hence, it was chosen to keep it at 1600 V, the same voltage from the previous iteration of the experiment [10].

Eventually, the single photo-electron charge was evaluated for the readout PMT. This was achieved by applying a lid to its photo-cathode and placing it on top of the two trigger scintillators. Then, two sets of data were acquired, one triggering on the PMT signal itself (with a threshold of $V_{th} = -10$ mV to reject noise), and another one using the external trigger to select only cosmic signals, namely Cherenkov photons emitted from the photo-cathode window. Typical signal shapes for the two processes are shown respectively in Figures (2.15) and (2.14).

For each run, the charge released in an event was evaluated by integrating the electric current over a time interval suitable to cover the entire signal. The current was obtained by dividing the acquired signal (in mV) by 50Ω , i.e. the resistance to which all lines in the experiment were adapted. Moreover, a similar integration was performed in a span preceding the signal formation, this allowed to estimate a charge pedestal due to a non zero baseline.

The charge histogram of the pedestal was then fitted by a Gaussian function. The mean extracted from the fit, re-scaled by a factor given by the ratio of the two time intervals, was subtracted from the signal charges in order to obtain an ‘offset-free’ distribution. The validity of this assessment was confirmed by observing the presence, in the charge histogram for the second data set, of a Gaussian peak centred at zero, caused by the prevalence of empty events over those with the emission of Cherenkov photons (see Figure (2.16)). This was due to the geometric configuration of the system, since the scintillating bars used to trigger the muons had a way larger surface than the PMT’s photo-cathode.

Then, the charge distributions from both runs were compared. It was found that there was an overlap between the tail of the auto-triggered data histogram and the charge distribution of the cosmic muon signals (Figure (2.16)). By looking at the single waveforms and at the average signals, it was possible to infer a threshold of 22.5 mV to expunge the cosmic signals, which usually were of greater amplitude, from the first set of data (Figure (2.17)). Eventually, the charge distribution of the remaining single photo-electrons was evaluated and fitted to a Gaussian model. In conclusion it was found

$$Q_{phe} = (1.7 \pm 0.3) \text{ pC}. \quad (2.10)$$

This result was later used to convert the charge distribution from the GEM signals into photo-electron counts.

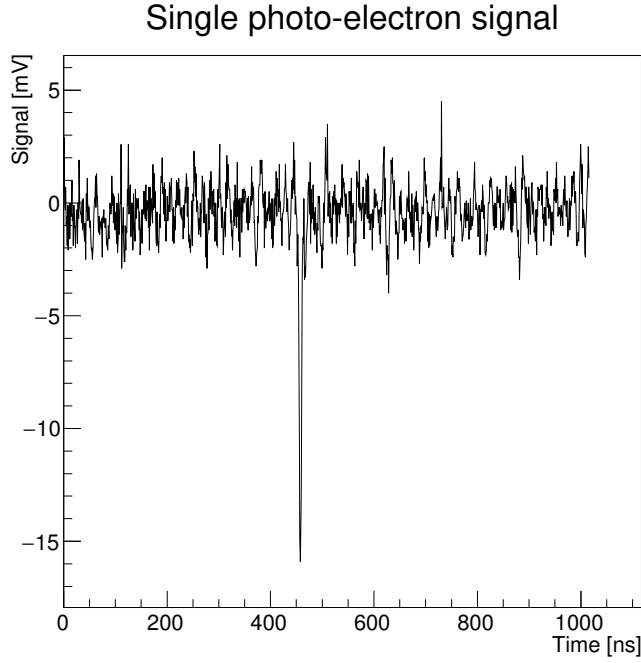


Figure 2.15: Typical signal from a single photo-electron in the readout PMT.

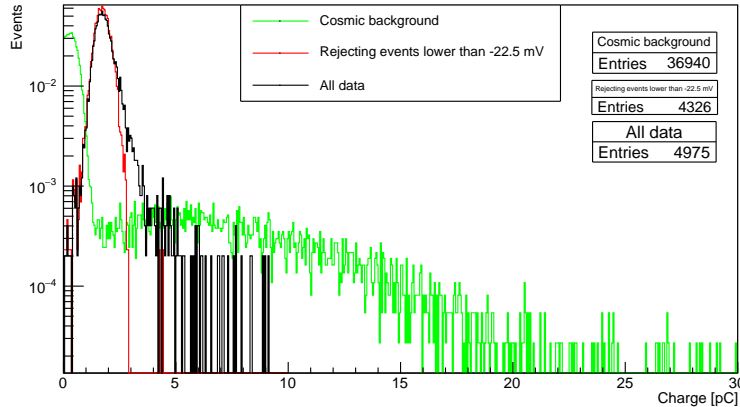


Figure 2.16: Charge distributions of single photo-electron signals and Cherenkov light events. “All data” refers to the events acquired in auto-trigger mode, before applying the rejection of signals coming from muons. All histograms are scaled to their number of entries.

2.3.3 MPPC 13360-6050CS

The Hamamatsu MPPC 13360-6050CS is an array of 14400 APDs on a $(6 \times 6) \text{ mm}^2$ surface with a fill factor of 74%. In this experiment, the MPPC is used to evaluate the light emitted from the de-excitation of the electrons in the atoms of the gas mixture. This instrument has been installed on the Hamamatsu C12332-01, a simple evaluation board for non-cooled MPPCs. A high-precision high voltage module for the MPPC can be found on this board alongside all the required communication ports. The high voltage module is mandatory to convert the input voltage coming from a low voltage power supply into a higher voltage, and it can be tuned via a software interface provided by Hamamatsu.

Since the gain function and the SNR are strongly dependent on the voltage supplied to the instrument, a voltage calibration for the MPPC will be shown §4.4. Increasing the voltage, the APD is subject to a transition from a linear mode to a proportional (Geiger) mode. The voltage in which this transition happens is called breakdown voltage, or V_b . Since it is supposed to work in Geiger regime, the main features of the MPPC are described using the *over-voltage*, which is the difference between the supplied

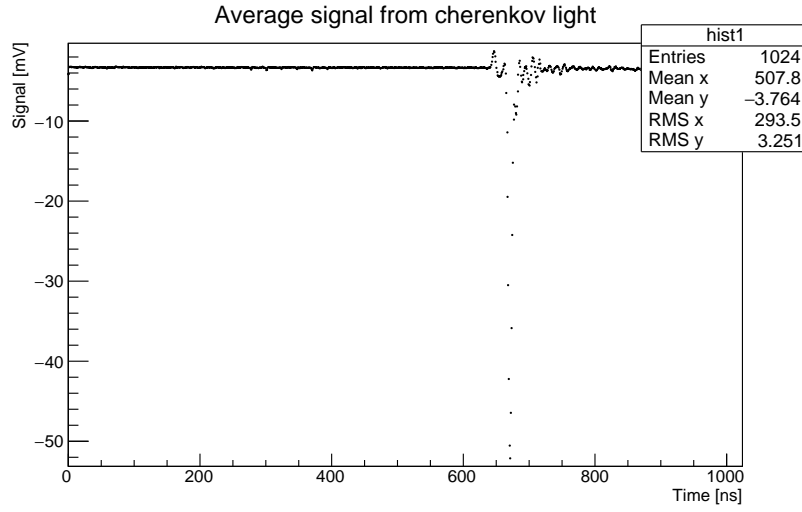


Figure 2.17: Average signal from Cherenkov photons on PMT photocathode.

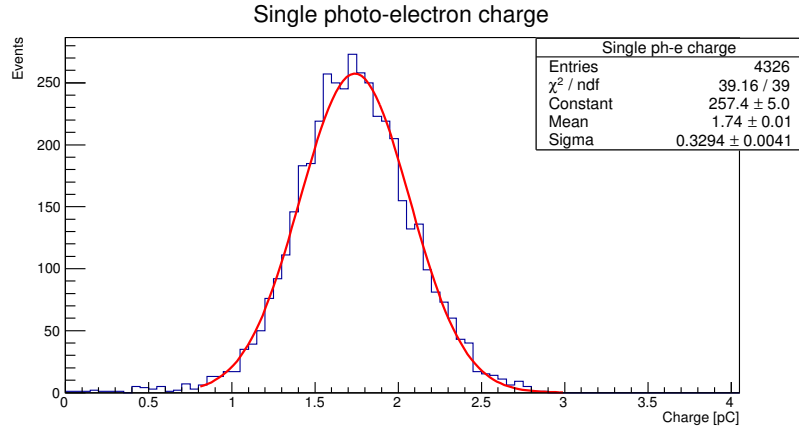


Figure 2.18: Charge distribution for single photo-electrons from the readout PMT.

voltage and V_b . Every APD works independently, resulting in a negligible deadtime during data acquisition, in low light condition. The efficiency of the light detection as a function of the photons wavelength is shown in Figure (2.19).

The target gas (He/CF4: 40/60) has its main spectral lines in two intervals: the main one, between 200 nm and 350 nm, and the secondary one, between 450 nm and 800 nm. This spectrum does not agree with the light detection efficiency curve of the MPPC, which has its maximum at 450 nm, where the MPPC's detection efficiency is around 40%, and this represents one of the main problems in data taking. The characteristic curves for the MPPC as functions of the over-voltage are shown in Figure (2.20).

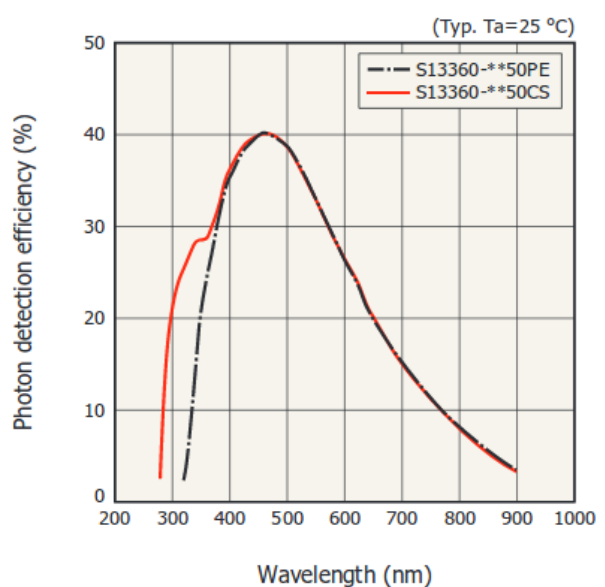


Figure 2.19: Light detection efficiency for the MPPC.

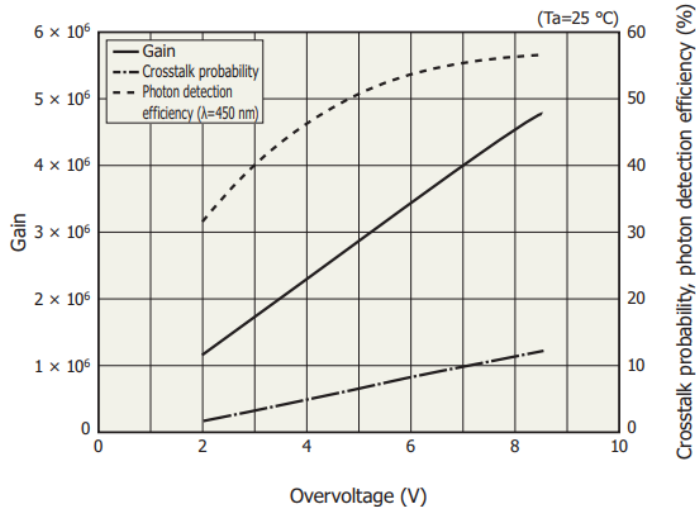


Figure 2.20: Characteristic curves for the MPPC.

The MPPC output is also dependent on the temperature, as its P-N junctions are affected by it, but it's possible to tune a compensation coefficient via the evaluation board on which the MPPC is mounted. This coefficient modulates the high voltage in order to reduce temperature effects.

2.4 Gas management

The gas has been managed remotely throughout the course of the experience as the storage tank is located on the roof of the laboratory building. The gas cylinder ports were connected to a networked flow-meter. From the laboratory, a PC connected to the same network was used to set the parameters of the gas flow. As an additional security measure, alongside the automated ports, a pair of knobs could be used to open or close the gas pipes. From there, the gas flowed through the detector and, after exiting the apparatus, the gas was sent outside through a bubbler, which was useful to monitor the gas flow, since the remote-controlled system was not calibrated, and also acted as one way valve to prevent contamination from the external atmosphere. In order to ensure that the proper mixture was inside the detector during its operation, we let the gas mixture flow for about 30 min before powering on the detector.

Chapter 3

Geant4 simulation

Geant4 (GEometry ANd Tracking) is a tool-kit for the simulation of the passage of particles through matter using Monte Carlo methods, developed by CERN. In this environment, a simulation of the experimental set-up was implemented to estimate the rate of cosmic muons that pass through the trigger system and make a comparison with theoretical expectations and the measured rate.

3.1 Simulation of the experiment

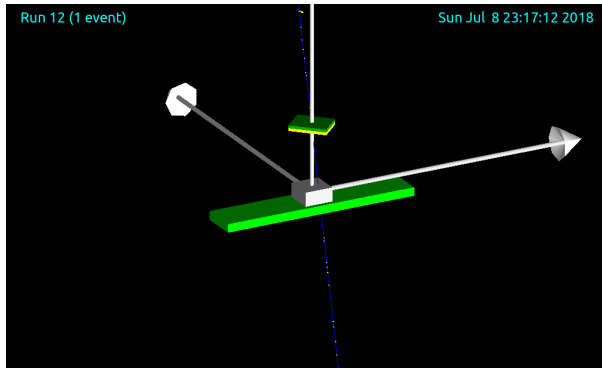


Figure 3.1: Simulation of a muon passing through the trigger system in Geant4. The geometry of the experiment can also be seen, from top to bottom: the A_2 (green) and the A_1 (yellow) scintillators, the GEM detector (white) and the *down* scintillator (green).

The starting point was to properly recreate the geometry of the experiment. To do so, only the part of the detector that effectively reveals the muons was implemented, as can be seen in Figure(3.1). In order to make the simulation as realistic as possible, the actual materials of the scintillators, and the gas inside the GEM detector, were set, but the internal structure of the GEM (all the foils and the holes, the electric fields etc.) was not reproduced, since it was not essential to our goal.

To optimise the results, the *physics list QBBC* was chosen.¹ The typical secondary cosmic ray distribution at sea level is [7]:

$$\frac{d^2I}{dSdt} = \cos^2(\theta) \sin(\theta) d\phi \quad (3.1)$$

where $\phi \in [0, 2\pi]$ and $\theta \in [0, \frac{\pi}{2}]$, and dS is the surface element.

The muons were generated with an energy of 3 GeV, which is the average energy of muons arriving to the Earth's surface [7], and according to the distribution (3.1). Moreover, an additional factor $\cos(\theta)$ was introduced to normalise the flux to an horizontal surface. In the end, the implemented distribution was:

$$\frac{d^2I}{dSdt} = \cos^3(\theta) \sin(\theta) d\phi \quad (3.2)$$

¹QBBC, provided by the Geant4 developer, is a package that allows to reproduce physics processes happening at energies over 1 keV (in fact under this energy it loses accuracy) and below 1 PeV, which are the correct ones for cosmic muons. [12]

A *Hit Or Miss* method was used together with a random number generator to generate the muons' trajectories according to the distribution in (3.2). Then, the origin point for each muon had to be chosen. In order to be as close as possible to what happens for real muons, the starting point was randomly generated on a spherical cap of radius $R = 1$ m, which is way larger than the size of the trigger system. Hence, the muons started from a random point on the spherical cap and moved toward the $A1$ scintillator.

In order to estimate the rate, all the particles which had passed through the trigger system had to be recorded, i.e. the coincidences among the $A1, A2$ and *down* scintillators, that have to be renormalised as will be explained in the following section. This was achieved by computing the amount of energy released by each muon of the simulation in each trigger component and increasing a counter when the energy release in one of the components passed a certain threshold. Several counters have been implemented: one for each scintillator, one for the coincidence between $A1$ and $A2$ and one for the entire trigger system ($A1, A2$ and *down*).

The distribution of the energy loss is a Landau, as can be seen in Figure(3.2). Since it was important to make the energy loss in the scintillators more realistic, the simulation code was modified to make the energy loss distribution broader, adding a Gaussian resolution to the energy loss distribution. This was due to the fact that, when a muon passes through a scintillator generating a count in the simulation, its energy loss depends on muon-matter interactions, which are reproduced by Geant4 itself. These interactions have a specific energy loss and involve a lot of secondary effects, producing an unrealistically narrow energy distribution (Figure (3.2) (left)). Hence, the energy deposited at every step was multiplied by a random number, distributed in the range $[0, \sigma]$ according to a Gaussian. This resolution σ could be set by the user and each random number was selected by another *Hit Or Miss* method. A value of 30% for the resolution was chosen in order to improve the comparison with experimental data, as it is discussed in section 3.2.2. An example of the energy distribution after the inclusion of this effect is shown in Figure (3.2 (right)).

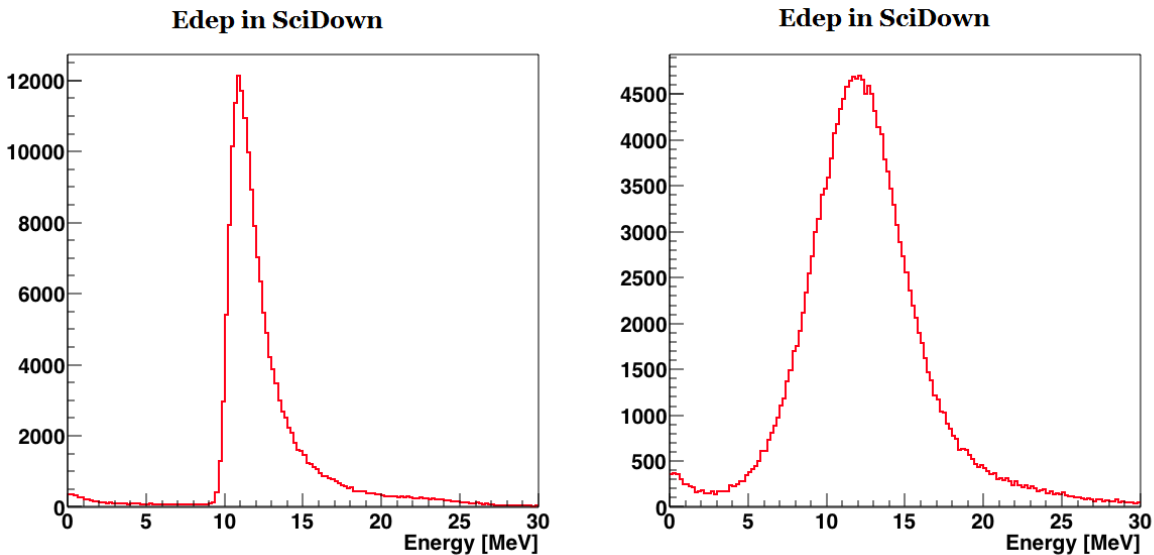


Figure 3.2: Energy deposit in the *Down* scintillator without resolution (left) and with a 30% resolution (right), both simulated running 1 million events. The left plot has a strongly asymmetric energy release, with a very small width, which makes it unrealistic, considering the age of our equipment. The distribution in the plot on the right is a more realistic approximation of the actual energy release distribution.

3.2 Analysis and results of the simulation

3.2.1 Trigger rate in the simulation

As already said in the introduction to this chapter, the main purpose of running the simulation in Geant4 was to compare the rate of cosmic rays passing through the trigger system to both the theoretical estimate

and the actual measurement. To do this, 1 million muons were used to increase the statistic significance of the simulation, whose results are reported in Table 3.1.

| Trigger system component | Number of counts |
|--|------------------|
| <i>A1</i> scintillator | 999864 |
| <i>A2</i> scintillator | 901475 |
| <i>Down</i> scintillator | 237482 |
| Double counts (<i>A1</i> + <i>A2</i>) | 901342 |
| Trigger counts (<i>A1</i> + <i>A2</i> + <i>Down</i> scintillator) | 236705 |

Table 3.1: Counts recorded by each component in the Geant4 simulation.

The next step was recording the counts from the *A1* scintillator, normalise them to its surface and compare this value, neglecting the angular dependence, with the expected number of muons at sea level in (2.3). From this comparison the characteristic time τ_{sim} of the simulation was obtained as

$$\tau_{sim} = \frac{N_{sim}^{ScintA1}/S}{F_0} \frac{[\text{ev}/\text{cm}^2]}{[\text{ev}/\text{cm}^2]} \text{s} \simeq 1.1 \cdot 10^6 \text{ s}, \quad (3.3)$$

where S is the scintillator surface and F_0 is the number of muons at sea level per square centimetre, that is reported in 2.2.3. The rate of muons in the trigger was computed dividing the number of counts recorded from the trigger system in the simulation by the characteristic time

$$R = \frac{N_{sim}^{trigger}}{\tau_{sim}} \frac{\text{ev}}{\text{s}}. \quad (3.4)$$

The error on the rate was estimated by running the simulation overestimating and underestimating the volume of the scintillators, and evaluated as

$$\Delta R_{sim} = \frac{R_{V+\sigma_V} - R_{V-\sigma_V}}{2}, \quad (3.5)$$

where σ_V is the error in the measurement of the scintillators' volumes. From the counts in Table 3.1 and τ_{sim} , the estimated rate of the simulation is

$$R_{sim} = 0.22 \pm 0.04 \frac{\text{ev}}{\text{s}} = 0.22 \pm 0.04 \text{ Hz}. \quad (3.6)$$

This value is not too far from the one experimentally measured minus the random coincidence and quite compatible to the one obtained from the theoretical computation, both reported in section 2.2.3, which are $R_{teo} = (0.26 \pm 0.02)$ Hz and $R_{exp-ran,exp} = (0.327 \pm 0.007)$ Hz.

3.2.2 Comparison of energy distributions in simulation and data

Another interesting analysis is the comparison between the charge released in the real scintillators and the energy release in the simulation. In order to do so, a set of measurements was taken for the *down* scintillator and for the sum of the *A1* and *A2* scintillators, acquiring 10^4 events triggered on the coincidence between these two signals, as described in §2.2. For what concerns the amount of energy accumulated in the simulation, it is remarked here that a resolution of 30% was introduced, to make it more realistic and spread it from a distribution which otherwise would have been very sharp (see §3.2.1).

In Figure (3.3) we show the superimposed distributions of the data, in blue, and of the Geant4 simulation, in black. Those distributions are normalised to the numbers of events, i.e. imposing that the value of the integral is 1. In order to compare the two distributions, the x scale of the data distribution was multiplied by the factor $\frac{P_{sim}^{max}}{P_{exp}^{max}}$, where P_{sim}^{max} is the x position of the peak and P_{exp}^{max} is the same for the experimental data.

As it is possible to see in Figure (3.3), the two distributions are not in good agreement with each other, especially in the tail, which is less pronounced in the simulation. Many efforts were made to reproduce the Landau tail of the data distribution varying the resolution of the simulation. Nevertheless, it was not possible to come to a definitive conclusion. Moreover, the distribution of the simulation also has some events at very low energy, which are not present in the data. However, the data have a cut-off at low charge that is due to the threshold chosen in section §2.2. Thus, the histogram does not start from

zero, but from a greater charge value. From this cut-off, it is possible, at least in principle, to infer an energy threshold for the simulation. Indeed, one could run many simulations with different values of the energy threshold, until the simulated distribution agrees with the data. Introducing this threshold in the code, one can expect improved results, both for the energy distribution and for the rate of muons in the trigger system.

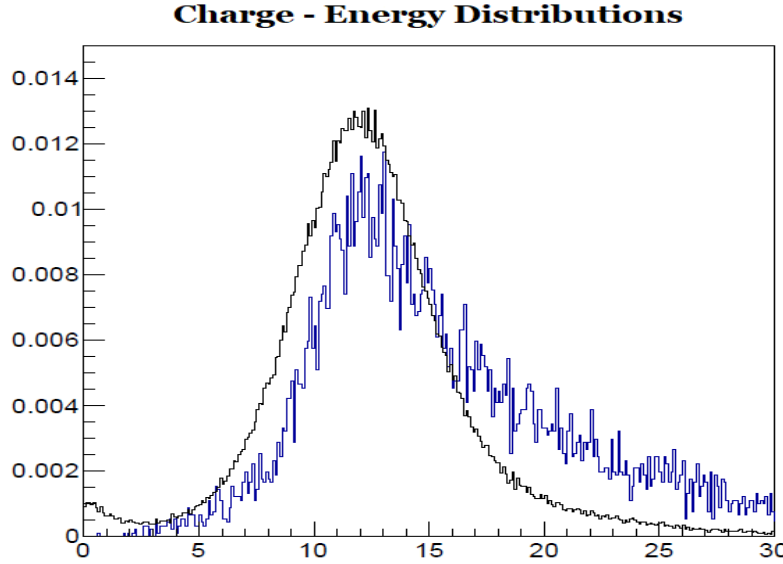


Figure 3.3: Comparison between charge in pC (blue) and energy in MeV (black) released in the *down* scintillator, both rescaled as described in the text and normalised to unity.

Chapter 4

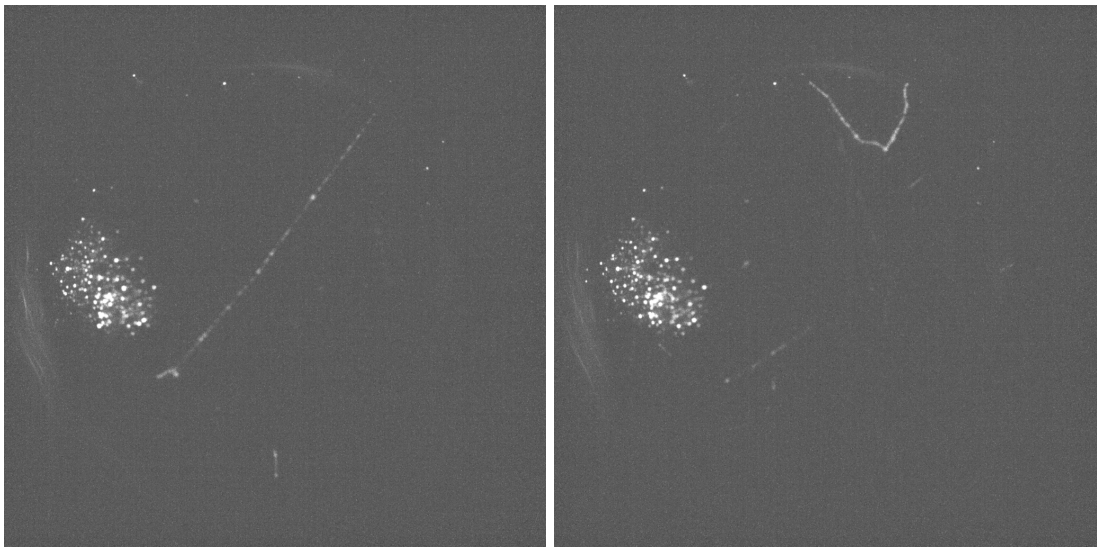
Measurements

Once the overall set-up of the trigger and read-out systems was completed, we activated the Triple-GEM detector to study the different signals readable with the PMT. Two sets of measurements were taken:

- 1 A scan in the voltage supplied to the GEM foils, V_{GEM} , from which we aimed to evaluate the number of photo-electrons detected.
- 2 A scan in the intensity of the drift field, E_{drift} . From this set we extracted a measurement for the electron drift velocity, the overall time resolution of the apparatus as well as the number of photo-electrons detected.

Calibration measurements for the MPPC were carried out in order to assess its dark noise and gain.

4.1 PMT: Review of detected signals



(a) Example of a muon track in the GEM. (b) Example of a δ track in the GEM.

Figure 4.1: CMOS camera images acquired after the repair procedures described in §A. Both show the presence of damaged sections, called *hotspots*, in the device.

4.1.1 Signals detected with external trigger

Using the trigger system described in §2.2, we were able to select signals generated in the GEM by muons from secondary cosmic rays. We expect these particles to transverse the detector, leaving a linear trail of ionisation clusters in the drift region, as seen in Figure (4.1a). The electrons in those clusters will be then transported and amplified by the GEM fields. Since the clusters are formed at different heights in

the drift gap, we could resolve the signal generated in the GEM from each cluster. Often this kind of events is preceded by a peak at fixed time, originated from the Cherenkov emission in the photocathode window of the PMT, as shown in Figure (4.2). The signals generated by the muons range between 10 mV and 100 mV in amplitude.

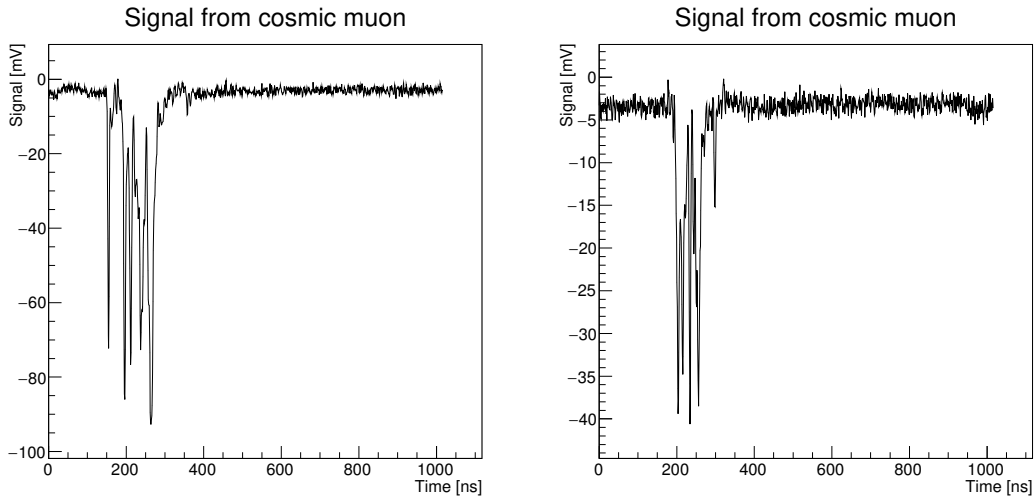


Figure 4.2: Examples of signals detected when using the external trigger. One can observe the presence of an extra spike in the left figure due to the aforementioned Cherenkov light.

4.1.2 Signals in auto-trigger mode

When the external trigger was disabled and the PMT itself was used as a trigger for the DRS acquisition, we were able to detect two different kinds of signals.

Large clustered signals

These events show the same pattern of clusters as those generated by cosmic muons, but are larger in amplitude, around 1 V. This forced the introduction of some attenuation in the DAQ system in order to properly acquire them (§2.1.2 and §2.1.3). The sources of these events are likely to be δ rays, electrons generated from near head-on collisions between massive charged particles, either from natural radiation background or other secondary cosmic rays, and atoms in matter [13, pgg. 30-31]. These processes liberate slow, short-ranged electrons with enough energy to induce other ionisation events in the detector gas mixture. These secondary ionisations are then picked up and amplified by the GEM. This hypothesis is consistent with the presence in the GEM of short and bright tracks, as seen in Figure (4.1b) and [5]. Moreover the greater intensity of these signals would be justified by the higher energy release of a slow electron, compared to that of a cosmic muon, which can be approximated with a minimum ionising particle. See Figure (4.3) for an example.

Hotspot signals

Another distinct type of signal was observed in the auto-triggered mode. These signals showed a single peak with no cluster structure and an amplitude of order 10 mV and were correlated to the so-called *hotspots*, as further elaborated on in §4.2.2. These are small regions on a GEM layer that have suffered some damage, and are therefore subject to continuous small discharges when a voltage is applied. These hotspots appear as small bright points in the CMOS images of Figures (4.1a) and (4.1b). An example of a *hotspot-generated signal* detected by the PMT is shown in Figure (4.4).

Signal from delta-radiation

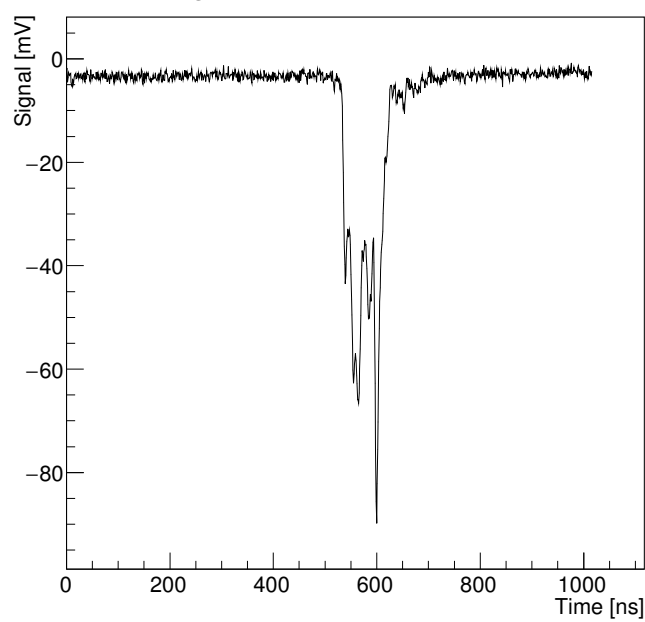


Figure 4.3: Example of a typical δ -ray signal. $V_{GEM} = 430$ V, Attenuation = -18 dB.

Hotspot signal

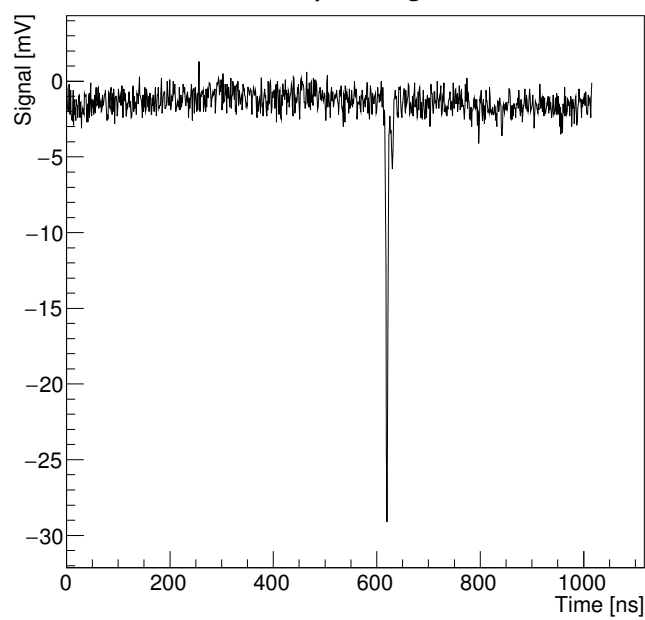


Figure 4.4: Example of a typical hotspot signal. $V_{GEM} = 430$ V. Attenuation = -6 dB.

4.2 V_{GEM} scan: readout with PMT

This first data set was taken fixing the electric fields outside the GEM layers, i.e. the drift and transfer fields (see §1.1.1 and §2.1.1), and varying the voltage between the two copper foils (V_{GEM}). These data were taken without using the external muon trigger, but triggering on the PMT itself at a threshold of -15 mV . Therefore, the signals acquired are those described in §4.1.2.

4.2.1 Photo-electron counts

The fields were set at

$$E_{drift} = 1000 \text{ V/cm}$$

$$E_{transf} = 2000 \text{ V/cm}$$

and V_{GEM} has been varied in the range [400, 460] V, proceeding by steps of 10 V, with 30 minutes long data acquisitions. For each voltage value the signal has been attenuated differently, in order to exploit the input range of the DRS in the best possible way (typical values were from -18dB to -26dB).

Then we evaluated the total charge collected by the PMT for every set, using the same method as described in §2.3.2 and multiplying by the appropriate factor in order to recover the non-attenuated values. The distributions were then fitted via a Landau function. An example distribution for $V_{GEM} = 410$ V and its best fit curve are shown in Figure (4.5).

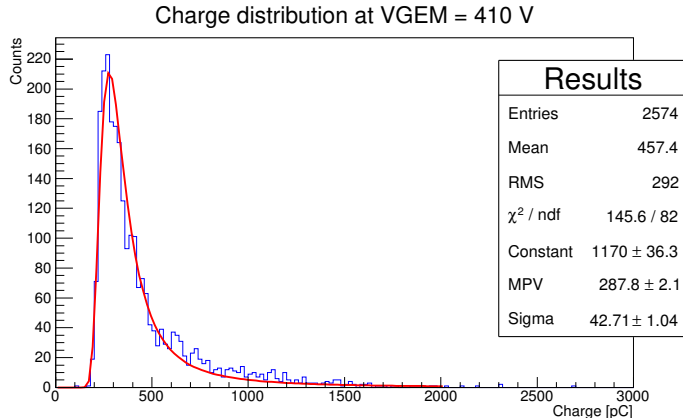


Figure 4.5: Example of a charge distribution for auto-triggered events.

Eventually, the MPVs of the single Landau fits were plotted together as a function of V_{GEM} . The charge values were then converted into photo-electrons using the single photo-electron charge measured in §2.3.2, and the statistical error was propagated accordingly (Figure (4.6)).

The data set corresponding to $V_{GEM} = 460$ V has been excluded as it showed an anomalous charge distribution. In fact when V_{GEM} was brought at 480 V one of the layers underwent a discharge event that rendered it inoperable (see Appendix A, for further details). So, it stands to reason that already at 460 V the device was not functioning properly, rendering the data useless.

As expected, the de-excitation light received from the GEM increases with the voltage supplied to the foils. However, we were unable to extract a measure of the gain of the device as the quantum efficiency of the readout PMT was unknown.

4.2.2 Distinction between δ -signals and hotspots

After obtaining the images of some signals via a CMOS sensor, Figures (4.1a) and (4.1b), it seemed mandatory to understand if the signals acquired in our auto-trigger configuration came only from ionising radiation (δ) or if they included also events generated by hotspots.

Since the discharges do not depend on the presence of a drift field in the ionisation gap, but are a mere consequence of a voltage being applied on the GEM foils, we expected to see hotspot signals even if $E_{drift} = 0$. In this setting, instead, all signals coming from ionisation should be suppressed, since the electrons wouldn't be carried to the multipliers.

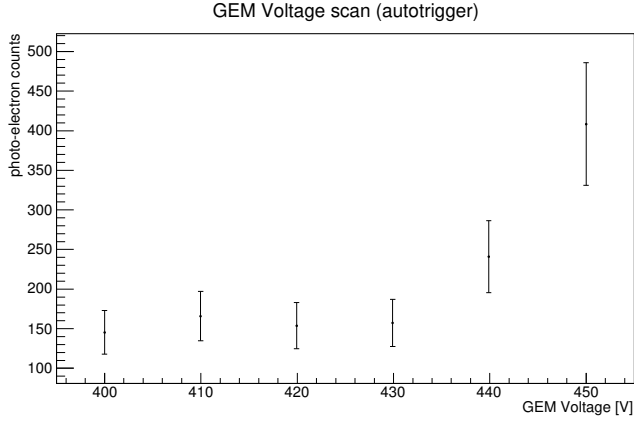


Figure 4.6: Number of detected photoelectrons at variable GEM voltages.

Thus, we acquired a set of data auto-triggering the PMT without drift field. The result was a much higher event rate (around 40 Hz against 3 Hz from the auto-triggered scan), but with a smaller average signal (an example is shown in Figure (4.4)).

The signal attenuation needed in the auto-trigger configuration with $E_{drift} \neq 0$ (see §4.2) was high enough to filter out the hotspot light. In fact, the difference in the event rates in the two configurations confirms this hypothesis. Hence, we can conclude that in the discussion above the presence of hotspots in the GEMs can be neglected.

4.3 E_{drift} scan: readout with PMT

This second data set was instead acquired with fixed GEM voltages and transfer fields, this time varying E_{drift} in order to study the time resolution of the whole GEM+PMT system. In these measurements we used the external trigger, thus observing signals generated by muons crossing the detector (see §4.1.1). We set

$$V_{GEM} = 430 \text{ V}$$

$$E_{transf} = 2500 \text{ V/cm}$$

and acquired data for $E_{drift} \in \{500, 1000, 1500, 1700\} \text{ V/cm}$. Due to the low trigger rate (see §2.2.3) and the small fraction of non-empty events (accentuated by the low light yield of the 40:60 He:CF4 mixture [10, 3]), these acquisitions were significantly longer in time than the ones exposed above, with durations from 4.5 to 7 hours¹. The data were used to study two different aspects of the detector's timing response: the width of the signal, which is correlated to the electron drift speed in the drift region, and the system's time resolution. Moreover, the deposited charge was also evaluated.

4.3.1 Signal width and electron drift speed

For each drift field intensity we evaluated the average signal over all the events in the data set. In all cases a common structure was identified, showing a signal of variable length, due to gas de-excitation light, and a fixed peak, generated from the Cherenkov signal (Figure (4.7)).

The duration of the main signal and E_{drift} is correlated to the drift velocity of the electrons in the lowest section of the GEM. We measured this interval, Δt , by comparing the time separating the 2 points at which the average signal was at 30% of its deepest peak. This number was used as an estimate for the signal length. Comparing Δt with the separation in time between points at 20% and 40% of the signal amplitude, a systematic error was assigned in the form:

$$\sigma_{\Delta t} = \frac{1}{2} (\Delta t_{20\%} - \Delta t_{40\%}) . \quad (4.1)$$

¹It would have been better to do longer acquisitions, since the statistical sample used in analysis was still barely 10^3 events. However, this wasn't possible because the pre-measurement set-up procedure (i.e. applying voltage to the detector and let the gas flow into it stabilise) required about an hour, and while acquiring data the voltage control interface had to be constantly monitored in order to prevent further damage to the GEMs, making it impossible to take data overnight.

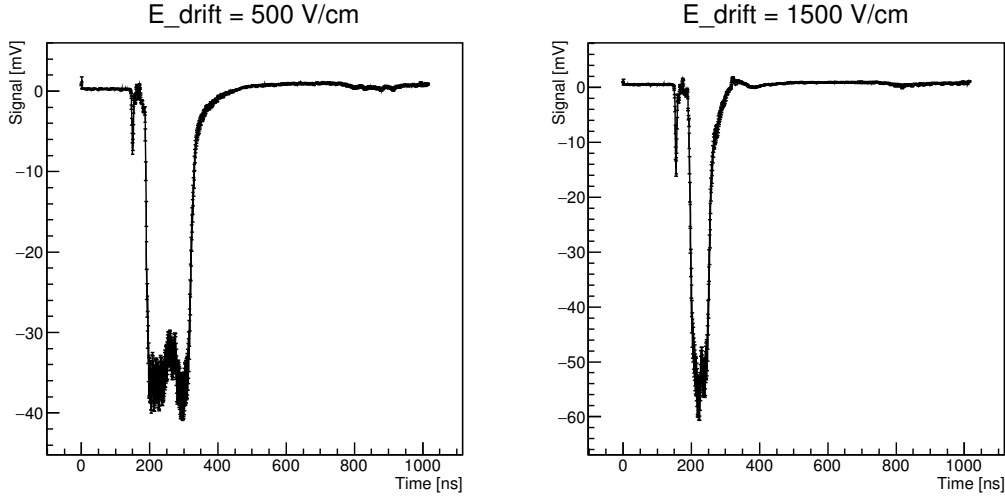


Figure 4.7: Average signals at $E_{drift} = 500$ V/cm and $E_{drift} = 1500$ V/cm. The duration changes significantly, while the Cherenkov peak stays in the same position.

The resulting points are reported in Table 4.1 and shown in Figure (4.8). A fit in the form

$$\Delta t(E_{drift}) = A + \frac{B}{E_{drift}},$$

was then performed to the experimental points.

| E _{drift} [V/cm] | Signal width [ns] |
|---------------------------|-------------------|
| 500 | 139.0 ± 4.0 |
| 1000 | 84.4 ± 4.0 |
| 1500 | 62.6 ± 4.1 |
| 1700 | 57.6 ± 3.7 |

Table 4.1: Measured signal lengths.

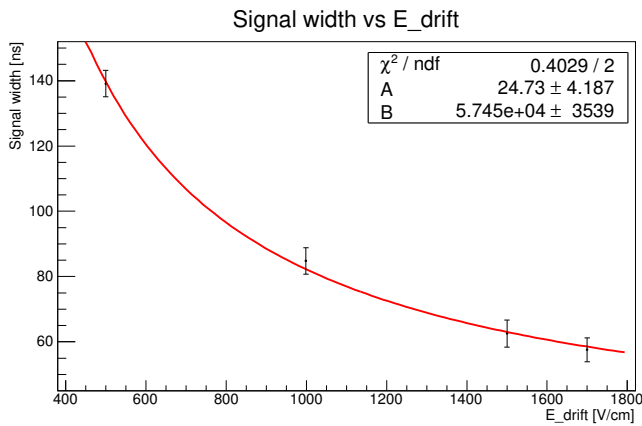


Figure 4.8: Width of the average signal as a function of E_{drift} . The superimposed fit was made via the function $f(x) = A + \frac{B}{x}$.

The functional form has been chosen considering that the signal duration must be inversely proportional to the electrons' drift speed, which is itself directly proportional to the drift field intensity.

The fit results are

$$A = (24.7 \pm 4.2) \text{ ns},$$

$$B = (57.5 \pm 3.5) \cdot 10^3 \frac{\text{ns} \cdot \text{V}}{\text{cm}}.$$

Furthermore, under the assumption that a muon forms ionisation clusters along its entire track in the drift gap, we may assume that the signal duration corresponds to the time taken by a ionisation electron near the cathode to cross the entire height of the drift region, which is $h = 3 \text{ mm}$. This allows us to give an estimate of the drift speed inside the GEM for the electrons as

$$V_{el} \simeq \frac{hE_{drift}}{AE_{drift} + B} \rightarrow (3.62 \pm 0.24) \frac{\mu\text{cm}}{\mu\text{s}} \quad \text{for a drift field of } 1 \frac{\text{kV}}{\text{cm}}. \quad (4.2)$$

This result is consistent in order of magnitude with the drift velocity of $7.2 \frac{\text{cm}}{\mu\text{s}}$ reported in [5] for the 60:40 He-CF₄ mixture at a similar drift field intensity.

4.3.2 Signal timing

In order to measure the time resolution of the entire GEM + PMT apparatus, for each value of the drift field, three timing distributions were extracted:

- a signal time, t_s distribution, collecting the times at which the PMT signal passed a fixed threshold of -10 mV . An example is shown in Figure (4.9).
- a trigger time, t_t distribution, storing the time instant at which the trigger reached a level lower than -225 mV .
- An interval, t_i distribution, containing the time span separating the two moments above for each event. The presence of a delay line, $\delta t = 762 \text{ ns}$, between the trigger system and the readout PMT was also accounted in this computation, using the formula $t_i = t_s - (t_t - \delta t)$.

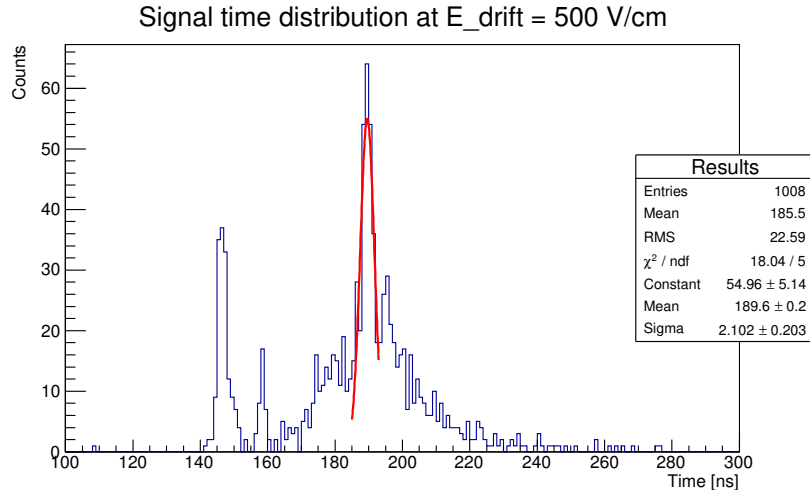


Figure 4.9: Example of a signal timing (t_s) distribution. The results of the superimposed Gaussian fit are summarised in the statistics box. We notice the Cherenkov peak around 150 ns, generated by muons crossing the photo-cathode window and preceding every other kind of signal (see §2.3.1).

These three distributions were fitted around their respective peaks with Gaussian functions in order to evaluate their means, $\mu_{t_{s,t,i}}$, and dispersions, $S_{t_{s,t,i}}$. Eventually, we extracted from these parameters a measurement for the time resolution of the system by considering:

$$S_{t_s}^2 = \sigma_{t_s}^2 + \sigma_{DRS}^2 \quad (4.3)$$

$$S_{t_t}^2 = \sigma_{t_t}^2 + \sigma_{DRS}^2 \quad (4.4)$$

$$S_{t_i}^2 = \sigma_{t_s}^2 + \sigma_{t_t}^2 \quad (4.5)$$

For each distribution, two sources of error were accounted for. One, $\sigma_{t_{s,t}}$, is the intrinsic time resolution of the experimental apparatus. The other, σ_{DRS} , is a contribution from the internal clock inside

the DRS board. The latter cancels out when subtracting two time measurements in the t_i distribution, since, in the same event, all channels are acquired simultaneously.

By inverting the previous system of equations one can extract

$$\sigma_{t_s}^2 = \frac{1}{2} (S_{t_i}^2 + S_{t_s}^2 - S_{t_t}^2) , \quad (4.6)$$

$$\sigma_{t_t}^2 = \frac{1}{2} (S_{t_i}^2 + S_{t_t}^2 - S_{t_s}^2) , \quad (4.7)$$

where (4.6) is the estimation of the time resolution we sought.

The obtained results are summarised in Table 4.2. As one can see, the time resolution is such that it is possible to identify the different ionisation clusters in the signals, which have typical lengths of 10s of nanoseconds, Figure (4.2). The last data point may indicate that timing performance degrades at high drift fields, further considerations are postponed to §5.3.

| E_{drift} [V/cm] | Time resolution [ns] |
|---------------------------|----------------------|
| 500 | 2.11 ± 0.17 |
| 1000 | 2.51 ± 0.15 |
| 1500 | 1.66 ± 0.31 |
| 1700 | 4.83 ± 0.22 |

Table 4.2: Measured time resolutions.

4.3.3 Photo-electron counts

In order to evaluate the charge released in the PMT anode after a muon transit, the same procedure of §4.2 has been applied. However, since the overall signal length changes with the drift field intensity, the integration gate for the current signal was hand-picked for each data set. An example of the resulting charge distribution is shown in (4.10).

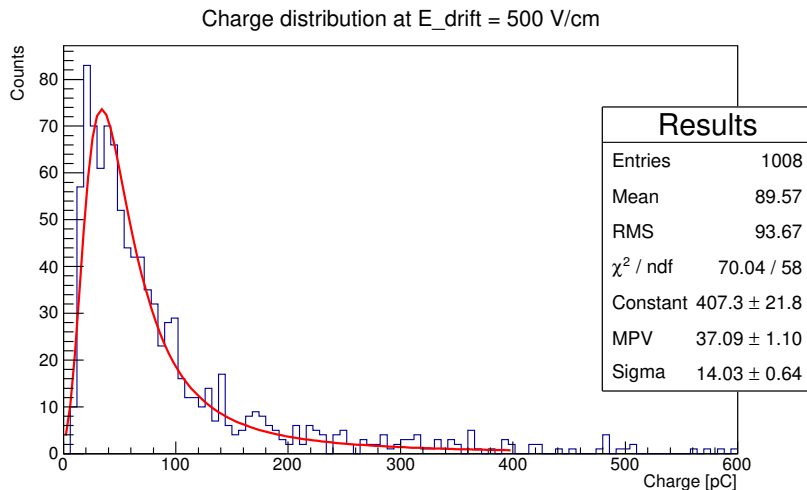
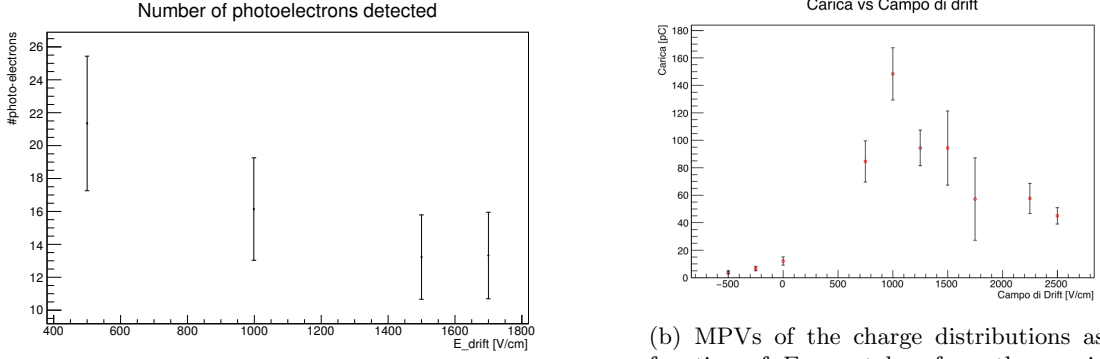


Figure 4.10: Charge distribution for muon signals at $E_{\text{drift}} = 500$ V/cm and its Landau fit.

For each distribution, a best fit curve has been evaluated using the Landau function. The MPVs of these fits have been plotted as a function of the drift field in Figure (4.11a), after rescaling for the single photo-electron charge found in §2.3.2.

The decreasing trend of these data is consistent with the same measures from [10] (see also Figure (4.11b)), and can be traced back to the fact that at higher drift field intensities the electron collection efficiency decreases, since more electrons are driven against the first GEM foil and stopped there. This issue is further discussed in relation to the time resolution in §5.3. The overall lower counts, with respect to the previous year data, can be traced back to the different light yield of the He:CF4 mixtures, respectively 60:40 in 2017 and 40:60 in this year.



(a) Number of photo-electrons generated in the PMT as a function of E_{drift} .

(b) MPVs of the charge distributions as a function of E_{drift} , taken from the previous iteration of the experiment, with a 60:40 He:CF₄ gas mixture [10].

Figure 4.11

4.4 MPPC calibration

A Multi-Pixel Photon Counter (MPPC) is a device designed for photon detection in low-light level conditions. It has a very high gain (around 10^6), and a negligible dead time thanks to its 14400 APD pixels. One of the tasks in this experiment is to evaluate the possibility of using an MPPC to collect the photons emitted inside the GEM apparatus. Before using the MPPC inside ORANGE, we need to estimate the intrinsic dark noise of the instrument and the gain as a function of the supply voltage sent to the device. We tried to collect data in a range that includes V_b , which is expected around (53 ± 5) V. The MPPC signal becomes unusable under a voltage of (53.2 ± 0.2) V due to electronic noise.

4.4.1 Dark noise

The dark noise background is constituted by the spontaneous signals generated inside the APDs. These signals come, most of the times, from a single electron-hole pair, then their peak is the same as the one generated by a single incident photon, as shown in Figure (4.12).

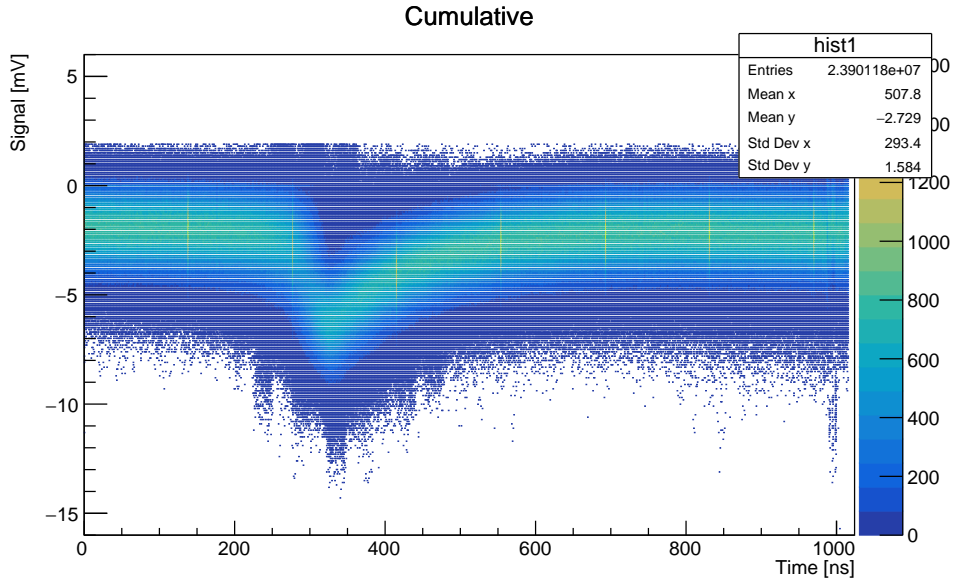


Figure 4.12: Single photoelectron signals in MPPC.

By collecting data with no incident light on the MPPC, one can evaluate not only the intensity of the dark noise, but also its rate. This measurement has been repeated with different threshold levels (3mV, 6mV, 9mV, 12mV). Using the DRS digitiser, a fixed number of events (from 100 to 50000, depending on

the rate itself, in order to avoid a too long collection time) has been collected for each supplied voltage, triggering on the MPPC signal itself. The collection time can be converted into the dark noise rate, while the integrated charge of the signals can be used to determine the increasing gain of the MPPC. The dark count rates taken at different thresholds are compared in Figure (4.13).

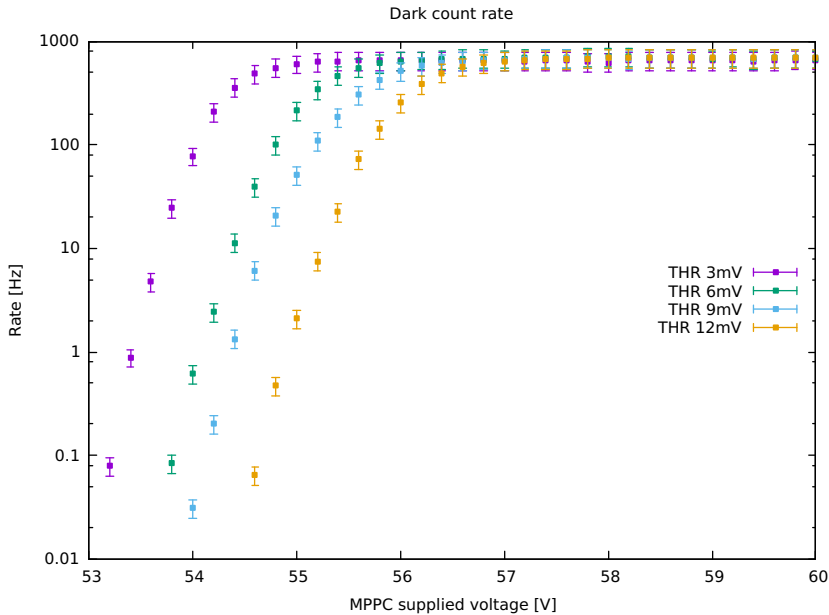


Figure 4.13: Measured dark count rates with different thresholds.

The estimated dark count rate in the plateau region is $R_{meas} = (646.1 \pm 21.0) \text{ Hz}$, compatible with the datasheet given range of $R_{theo} = [500, 1000] \text{ Hz}$.

4.4.2 Gain and RC filter

Scanning through all the possible values of supplied voltage for the MPPC, it has been noticed that the value of the signal baseline depended on the supplied voltage itself. Despite this not being a problem during the data acquisition, it is a drawback in data analysis.

When the baseline of the signal switched from negative to positive values, errors occurred in the charge integration algorithm. It was possible to correct this issue both via software revisions and via hardware corrections. The hardware correction, which is the simplest solution, has been chosen: an RC filter has been added after the MPPC output to remove the DC component of the wave, resulting in a stable baseline for the signal, scanning through all the supplied voltages. The RC filter is a high-pass filter, therefore it is possible to avoid that components of the signal are eliminated by setting the cutting frequency of the filter on a sufficiently low value.

The chosen values for the circuit were $R = 100k\Omega$ and $C = 22nF$, resulting in a cut frequency equal to

$$f_{cut} = \frac{1}{2\pi RC} = (72.3 \pm 3.6) \text{ Hz}. \quad (4.8)$$

Even if the range of the cut frequency is really short and much lower than the characteristic frequency of the MPPC signal, an attenuation was introduced by the filter. Through the charge distributions we could evaluate the proportionality between the filtered signal and the non-filtered one. Scanning all the possible values for the MPPC supply voltage, the integrated charge has been measured both for filtered and non-filtered signals. Data are shown in Figure (4.14), after having been fitted to straight lines.

The results of both linear fits, with $f(x) = mx + q$, are shown in Table (4.3).

These two lines are useful also to evaluate the point in which the gain of the MPPC is zero, which is the transition point from linear to Geiger mode for the MPPC. The voltage corresponding to a null gain is the breakdown voltage, V_b . From the fit results we can extract the zero-gain point for both filtered and non-filtered signals, resulting in the values shown in Table (4.4).

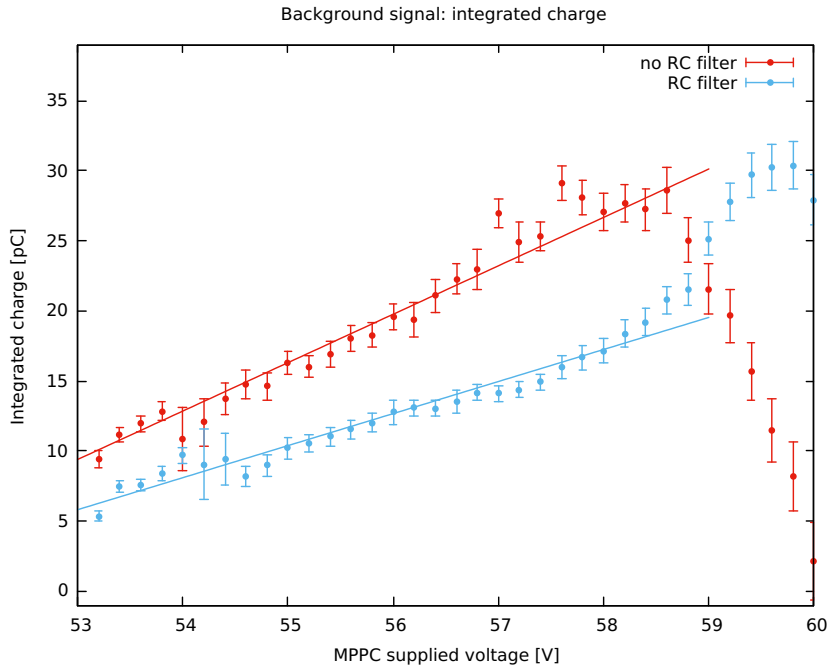


Figure 4.14: Dark count integrated charge as a function of the MPPC supplied voltage, together with a linear fit performed in the range [53, 58] V.

| | Non-filtered signal | Filtered signal |
|----------|--------------------------------|--------------------------------|
| m | $(3.45 \pm 0.16) \frac{pC}{V}$ | $(2.29 \pm 0.11) \frac{pC}{V}$ |
| q | $(-173.68 \pm 8.99)pC$ | $(-115.36 \pm 5.92)pC$ |

Table 4.3: Linear fit results.

| | Non-filtered signal | Filtered signal | Datasheet |
|-------|---------------------|---------------------|---------------|
| V_b | $(50.28 \pm 2.59)V$ | $(50.45 \pm 3.50)V$ | $(53 \pm 5)V$ |

Table 4.4: Zero-gain point values for MPPC integrated charge.

The measured V_b values are compatible with each other, and compatible also with the datasheet given value.

Chapter 5

Results

In this chapter the main results from the measurements exposed in §2, §3 and §4 are reported.

5.1 Cosmic ray rate

The rate of cosmic muons crossing our trigger system has been evaluated in three different ways. First, a theoretical computation has been carried out in order to obtain an expected value to use as reference for the actual measurements. This was useful to determine whether the scintillators and the related electronic circuitry were functioning properly or not, and in particular to check if the working points of the PMTs and the discriminator thresholds were set in a sensible manner. On top of that, the GEANT4 simulation, besides being a useful exercise itself, provided another estimate of the same quantity, so that the three procedures could be cross-checked. The results are thereby reported briefly in Table 5.1, where we can see that the three determinations are in good agreement with each other.

| Source | Cosmic ray rate [Hz] |
|---|----------------------|
| Theor. computation | 0.24 ± 0.03 |
| GEANT4 | 0.22 ± 0.04 |
| Measurement (excluding accidental coincidences) | 0.327 ± 0.007 |

Table 5.1: Recap of the trigger rate determination with different methods.

5.2 Single photo-electron charge

The next preliminary measurement has been the determination of the charge released by a single photo-electron in the readout PMT. This was done by obscuring the photo-cathode window, supplying the PMT with voltage and acquiring signals triggered on the PMT itself. The trigger threshold was set at $V_{thr} = -10$ mV in order to filter out thermal noise. Filtering out the signals from Cherenkov light on the photo-cathode as described in §2.3.2, the result of the Gaussian fit performed on the charge distribution is

$$Q_{phe} = (1.7 \pm 0.3) \text{ pC} \quad (5.1)$$

5.3 Timing of the GEM+PMT apparatus

Our first goal was to study the time response of the entire experimental apparatus for variations of the drift field. Two different aspects have been analysed: the duration of the average signal and the time resolution of the entire set-up.

We have observed that the average signal decreased with the drift field, as expected, and were able to extract an estimate for the electron drift velocity inside the detector, obtaining

$$V_{el} = (36.2 \pm 2.4) \frac{\mu\text{m}}{\text{ns}}$$

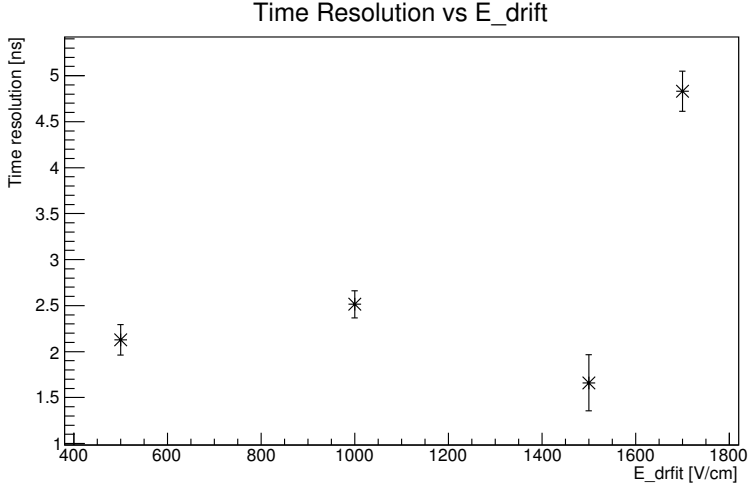


Figure 5.1: Time resolution as a function of E_{drift} .

for a drift field of $1 \frac{\text{kV}}{\text{cm}}$. This result is reasonably close to what has been reported in [5].

Then, the time resolution of the signal σ_{t_s} was studied, finding values of the order of a few nanoseconds for every E_{drift} . However, at $E_{drift} = 1700 \text{ V/cm}$, the value of σ_{t_s} is approximately twice as big as for the other drift field intensities (see Figure (5.1)). As already mentioned, we are still able to resolve the single ionisation clusters inside the drift gap, which produce signals of 10s of nanoseconds each.

The last data point may be explained by considering the loss of electron collection efficiency at high drift fields. In fact, if some electron clusters are driven onto the copper layer instead of being pushed through the GEM holes, there might be bigger fluctuations in the light production and thus in the signal timing. This hypothesis seems to be confirmed by the decrease of photo-electron counts at the same drift field intensity (Figure (4.11a)).

5.4 Results in MPPC calibration

The MPPC calibration has been a success. The breakdown voltage, V_b , was found to be (50.38 ± 3.04) V, while the value given by the datasheet was (53 ± 5) V. The dark count rate for the APD array has been measured with different thresholds, resulting in a rate of (646.1 ± 21.0) Hz, well within the datasheet given range of $(500, 1000)$ Hz. The RC filter with a low cut frequency added to the output circuit has been very useful both for the extrapolation of V_b and for the stabilisation of the signal baseline. If an even better calibration is needed, among the other possible measurements to characterise the MPPC there is certainly the study of known signals through the use of a pulsating LED as benchmark.

The study of this device has highlighted several unavoidable problems occurring during data acquisition: the APD pixels of the MPPC become less sensitive decreasing the over-voltage, and this could cause the loss of signals under a certain threshold. In this case, signals with low intensity cannot be distinguished from the pedestal. On the other hand, a high over-voltage could produce overwhelming avalanches inside the APDs and therefore the MPPC saturation. A reasonable compromise between those two situations may not exist if we are trying to measure a wide spectrum of incident light and, even if this is not the case, finding the best supply voltage for the MPPC is not trivial.

Besides the MPPC intrinsic saturation, the DRS digitiser has a limited input acceptance: input signals must be smaller than 500mV. To measure a muon signal in external trigger we have to set a high over-voltage for the MPPC, resulting in saturating signals for every delta ray passing through. The saturating signals are much greater than 500mV, thus they can't be sent to the DRS. To have output signals in the acceptance range we must choose a lower over-voltage, which again makes muon signals indistinguishable from the background.

Fortunately, choosing different trigger conditions (PMT-trigger or external trigger) the device will collect different light spectra: δ ray signals using the PMT-trigger, muon signals using the external trigger. Nevertheless, working with two different set of MPPC parameters for the two different spectra is mandatory, and in this case a double calibration may be needed to use the device properly.

Conclusions

In the course of the reported study, the set up of an optically read out triple GEM was implemented.

In order to isolate cosmic muons as a test source, a trigger system based on plastic scintillators and photo-multiplier tubes operating in coincidence was devised and characterised. Its correct functioning was verified by computing an expected trigger rate from the known distribution of cosmic muons at sea level and comparing it with experimental data. Moreover, a Monte Carlo simulation of the trigger system was developed as an additional way to estimate the expected trigger rate with respect to the experimental evidence.

Two optical read-out systems, a classic PMT unit and a MPPC, were mounted on the experimental apparatus and their performance characterised. Once all these operations were completed, the entire detector was brought on-line and data from cosmic muon events as well as δ background were collected. Due to several technical issues, we were forced to interrupt these acquisitions prematurely. Nonetheless, we were able to extract an estimate for several quantities of interest regarding the detector's properties, chiefly a measure for the time resolution of the apparatus and for the drift speed of the electron in the gas mixture.

The technical issues mentioned before occurred when the MPPC calibration was completed, rendering impossible to collect data simultaneously with the PMT and the MPPC. Despite this, the calibration returned enough information to say that this specific MPPC device is not a suitable choice to detect photons inside the GEM apparatus: as a matter of fact, the smaller dynamic range, the lower detection efficiency, the lower time resolution of the signal, and the smaller effective surface, make this device a bad choice even to replace a standard PMT in our experiment.

Appendix A

Recovery of a GEM layer

During the voltage scan for V_{GEM} , the device underwent a discharge due to the excessive applied voltage. As a result, the lowest of the three layers was damaged and appeared to be short circuited, rendering the experiment unserviceable. In order to fix this issue, we applied the method of a “burn test” proposed in [14] and [15], to remove carbonised impurities and other extraneous materials from a GEM layer by inducing a controlled discharge in the damaged section of the detector. Thus, after applying a bypass to the protection resistor of the damaged foil, we proceeded to supply it with a voltage drop in increasing steps up to 1000 V. At this point, a discharge phenomenon was generated in the foil, along with the emission of sound and visible sparks from the GEM. This destructive process supposedly removed the damaged surface by flaking it off the foil and restored the proper resistance between the faces of the GEM layer. In fact, the device was returned to its normal functioning, as all the data pertaining the drift field scan were taken after this operation. It is remarkable that further shocks from the power supply, namely two short black-outs in the laboratory, seemed to have no effect on the GEM functioning. In order to test immediately if the reparation had succeeded, the detector has been shortly operated at LNF, where the repairs had taken place, with a gas mixture of 60:40, and reading the light emission with a CMOS-based sensor (like the one described in [2], [3] and [4]). Two of the images that have been acquired are showed in Figures (4.1a) and (4.1b).

Bibliography

- [1] F. Sauli, The gas electron multiplier (GEM): Operating principles and applications, *Nuclear Instruments and Methods in Physics Research Section A: Accelerators, Spectrometers, Detectors and Associated Equipment*, **805** (2016), 2-24
- [2] M. Marafini, V. Patera, D. Pinci, A. Sarti, A. Sciubba, E. Spiriti, "High granularity tracker based on a Triple-GEM optically read by a CMOS-based camera", *JINST*, **10**, 2015, p. 12010, doi: 10.2967/jnumed.115.160481
- [3] M. Marafini, V. Patera, D. Pinci, A. Sarti, A. Sciubba, E. Spiriti, Optical readout of a triple-GEM detector by means of a CMOS sensor, *Nuclear Instruments and Methods in Physics Research Section A: Accelerators, Spectrometers, Detectors and Associated Equipment*, Volume **824**, 2016, Pages 562-564, ISSN 0168-9002, <https://doi.org/10.1016/j.nima.2015.11.058>.
- [4] M. Marafini et al., "ORANGE: A high sensitivity particle tracker based on optically read out GEM," *Nucl. Instrum. Methods Phys. Res. A, Accel. Spectrom. Detect. Assoc. Equip.*, vol. **845**, 2017, pp. 285–288, doi: 10.1016/j.nima.2016.04.014.
- [5] D. Pinci *et al.* High resolution TPC based on optically readout GEM, presentation at seminar: "Tecniche sperimentalni di rivelazione diretta di DM", June 2018. Available at: <https://agenda.infn.it/conferenceDisplay.py?confId=15988>, accessed 02/07/2018.
- [6] F.A.F. Fraga, L.M.S. Margato, S.T.G. Fetal, M.M.F.R. Fraga, R.Ferreira Marques, A.J.P.L. Policarpo, Luminescence and imaging with gas electron multipliers, *Nuclear Instruments and Methods in Physics Research Section A: Accelerators, Spectrometers, Detectors and Associated Equipment*, Volume **513**, 2003, Issues 1–2, Pages 379-387, ISSN 0168-9002, <https://doi.org/10.1016/j.nima.2003.08.066>
- [7] M. Tanabashi et al. (Particle Data Group), Cosmic ray review, *Phys. Rev. D*, **98**, 2018.
- [8] M.N. Torchia, "Development of a tracker based on GEM optically readout", master thesis (2016), url: "<https://cds.cern.ch/record/2289206>", presented 20 Jan 2017.
- [9] M.M.F.R. Fraga, F.A.F. Fraga, S.T.G. Fetal, L.M.S. Margato, R.Ferreira Marques, A.J.P.L. Policarpo, The GEM scintillation in He–CF₄, Ar–CF₄, Ar–TEA and Xe–TEA mixtures, *Nuclear Instruments and Methods in Physics Research Section A: Accelerators, Spectrometers, Detectors and Associated Equipment*, Volume **504**, 2003, Issues 1–3, Pages 88-92, ISSN 0168-9002, [https://doi.org/10.1016/S0168-9002\(03\)00758-7](https://doi.org/10.1016/S0168-9002(03)00758-7).
- [10] C. Bellenghi, E. Bossio, G. Frattari, J. Cerasoli. I. Longarini, "Studio di un rivelatore tripla-GEM in lettura ottica" (2017) https://drive.google.com/open?id=1fpGQQp8vkVXo_vwiBojLaelKcrhY4iK
- [11] DRS Evaluation Board User's Manual, url: https://www.psi.ch/drs/DocumentationEN/manual_rev51.pdf, accessed 05/07/2018.
- [12] *Physics List Guide*, Geant4 Collaboration
- [13] G. F. Knoll, *Radiation detection and measurement - 4th ed.*, (2012), published by Wiley & sons Inc. (NJ). ISBN: 978-0-470-13148-0
- [14] M. Kalliokoski, T. Hilden, R. Lauhakangas, P. Karppinen, T. Karppinen, R. Turpeinen, J. Heino, E. Tuominen, Detection and Removal of Short-circuits on GEM-foils, *Physics Procedia*, Volume **37**, 2012, Pages 464-471, ISSN 1875-3892, <https://doi.org/10.1016/j.phpro.2012.02.394>.
- [15] Muhammad Tahir, Muhammad Zubair, Tufail A. Khan, Ashfaq Khan, Asad Malook, Gas electron multiplier (GEM) foil test, repair and effective gain calculation, *Results in Physics*, Volume **9**, 2018, Pages 580-584, ISSN 2211-3797, <https://doi.org/10.1016/j.rinp.2018.02.011>.